University of Rome

"LA SAPIENZA"

Biophysics PhD School

XVII Course

"Study and realization of a high resolution gamma camera prototype for Scintimammography in Nuclear Medicine, inside I.M.I. project "

Supervisors: Prof. Alfredo Colosimo

Prof. Roberto Pani

Student: Dr. Maria Nerina Cinti

Academic Year 2003-2004

Acknowledgement

This work was supported by “Integrated Mammographic Imaging”, project, law 6/82 (art. 10).

The author thanks Prof. Roberto, Dr.ssa Rosanna Pellegrini, Dr.ssa Margherita Betti, Dr Paolo Bennati and Dr. Giuseppe De Vincentis for essential scientific and moral support and the friendship.

The author thanks Dr. Claudio Bonifazzi, Dr. Livio Finos and Mr. Valerio Muzzioli, University of Ferrara, for the collaboration about the development of new statistical technique of image analysis.

Thank you to Dr. Giorgia Iurlaro and to Dr. Livia Montani for the important collaboration during the realization and the calibration of the gamma camera prototype.

The author likes to address a thought to Prof. Stan Majewski, Jefferson Laboratory-Newport News-Va-USA, and to Prof. Mark Williams, University of Virginia-USA, for the collaboration and the helpfulness, also of their staff.

Finally a particular thank-you to Prof. Alfredo Colosimo and all Teaching Staff of the Biophysics PhD School for the patient, the attention and the precious advises.

..and thank-you to all “poor mice” in the world.

INTRODUCTION

Breast cancer and mammography

Breast cancer is most frequent women neoplasia, with more than 800.000 new diagnosed cases every year in the world. Currently in Italy 24,000 women for year are taken ill with breast cancer and approximately 10.000 of them die. The incidence of breast cancer is increasing in all countries, with a mean annual increment of 2% in the America North and Western Europe.

The pathogeneses of the breast carcinoma is no well know. In fact, individuation of a continuous process from a preneoplastica lesion to invasive tumor, based on progressive genetic and molecular alterations, does not exist. Probably in situ ductal carcinomas and atypical hyperplasias represent preneoplastiche lesions, since in a consisting number of women such lesions strongly manifest a potentiality to degenerate in an invasive carcinoma.

The more reliable theory about propagation of breast cancer cells is based on a casual diffusion mainly by blood vessels toward to lymphatic system and to other organs at the same time. The positive diagnosis on neighboring lymph nodes represents therefore an probability index about metastasis presence. The studies indicate the lack of influence of axillary lymph nodes treatment on cancer evolution, demonstrating that axillary lymph nodes haven't an anti-cancer positive function, that is they are not an instrument of defense about tumor development.

Basing on current experimental and clinical data, the natural history of breast cancer may be outlined: the carcinoma is initially monoclonal and subsequent mutations produce a wide spectra of subsets with different proliferation activity and response to hormones action. After twenty duplications, at 1 mm dimension, the tumor get to blood and lymphatic circulatory system, with high possibility to produce metastasis. The tumor is usually diagnosed when it has a diameter ranged from 1 to5 cm, corresponding to approximately 30-37 duplications.

Since duplication time is approximately 40-310 days (depends on patient age), tumor biological history is already long at the moment of diagnosis. In fact, 7-9 years are necessary to produce a lesion with 1 cm^3 size and to develop metastasis. After tumor diagnosis, 10-15 duplications cause the patient dead. A breast neoplasia 0.5 cm size, that is identifiable only with the mammography, is classified in initial stage but it is really a

biologically old tumor, whose premature location does not constitute a recovery guarantee. So the slow pre-clinical stage, that characterized the history of breast carcinoma, permits to assume that the disease often is generalized in microscopically dimension, if the dimension of the principal cancer is 1,5 cm. The high number of survivor patients after treatment with surgery and/or radiation therapy is probably due to the slow evolution of micro-metastasis rather than to complete extirpation of in situ tumor.

The life time of a woman with breast cancer may be foretold on the base of disease stage at the diagnosis time. An early diagnosis allows different therapeutic approaches, with a greater success.

The mammography represents the principal screening methodology for tumor identification in pre-clinical stage. Clinical trials demonstrate that the mammographic screening may reduce meaningfully mortality for such pathology and also to concur less aggressive therapeutic approaches, like conservative surgery for instance. In screening techniques, in order to estimate the diagnosis ability of an adopted technique, the evaluation of Positive Predictive value (PPV) is extremely useful. PPV is defined by PPV = TP/(TP+FP), where TP and FP are the number of true positive and false positive diagnosed cases respectively. Recent studies have demonstrated that the cumulative incidence of false positive results is equal to 49%. Such value changes by a minimum of 20% to a maximum of 60% in function of patient age. In particular patients with dense breast, breast prostheses and previous surgical or radiotherapy treatments, false negative incidence by mammography is about 25-30%.

The low PPV values require the necessity of other clinical investigations based generally on core biopsy , that in approximately 75% of treated cases they reveals like benign the suspicious lesions. The figure 1I shows two mammography images of suspicious lesions. For anomalous mass on the left, generally the core biopsy allows a correct diagnosis; for micro-calcifications the low image contrast and reduced dimensions of lesions do not allow neither to a precise localization neither an accurate diagnosis and highlight the necessity to introduce other diagnostic techniques.

In addition to other imaging techniques, like echography, echography Color Doppler, TC and NMR, the scintimammography was introduced.

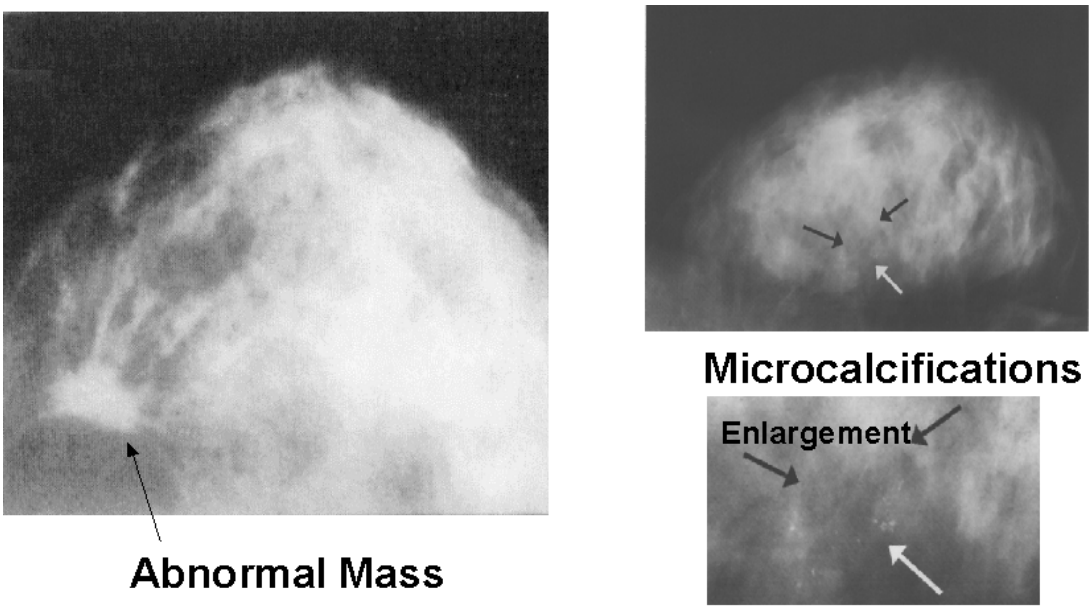

Figure 1I: Mammography images. On the left an abnormal mass is shown, on the right, micro calcifications are evident.

Scintimammography with ^{99m}Tc MIBI

Imaging in Nuclear Medicine is based on radiotracer, essentially gamma (Single Photon Emission - SPE) and β+ (Positron Emission Tomography- PET) emitter. A photodetector for SPE, like Anger Camera, is deputy to reveal radiotracer bio-distribution, in order to evaluate physiological function of individual organ in the body.

So, while a RX image substantially represents the absorption coefficients to X-ray of the tissues interposed between RX source and detector, producing anatomical information essentially, in SPE diagnostic in Nuclear Medicine, the information is strictly functional, because takes advantage on radiotracer peculiarity to create uptake in interest zones. The figure 2I shows a sketch of a breast cancer with micro calcifications, like shown in figure 1I. The scintigraphic image would reproduce the complete tumor, while the mammography underline only the secondary effect of tumor presence, the micro calcifications.

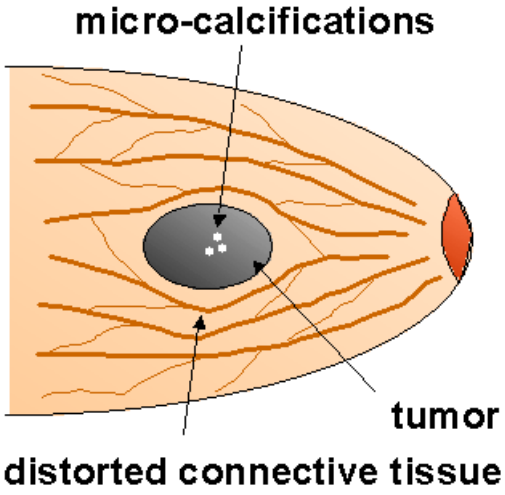

Figure 2I: Sketch of a breast tumor with micro calcifications

99mTc methoxyisobutil isonitrile

99mTc methoxyisobutil isonitrile (MIBI) is mainly used radiotracer for myocardium scintigraphy. In 1987 Muller observed uptake in pulmonary metastases coming from thyroid cancer. Although the first observation of uptake in breast carcinoma was in 1992, in 1994 Khalkhali and Waxman studies highlighted the nuclear medicine role in breast carcinoma diagnosis, producing the approval by Food and Drug Administration (FDA) in June 1997 of breast cancer diagnostic with MIBI tracer. The mechanism of radiotracer uptake in carcinoma cells is still in study. The MIBI, a small lipophilic cell positively charged at physiologic pH, is taken up in cytoplasm and mitochondrion and its absorption is due to voltage generated between cellular membrane and mitochondrion. The trans-membrane negative voltage guides 99mTc MIBI and approximately 90% of the radiotracer activity is found in mitochondrion. It can be extruded by Ca++ pump.

Delmon-Moingeon was the first one to demonstrate MIBI uptake increasing in cancer cells, while Piwnica-Worms observed that tracer is a substrate of trans-membrane glycoprotein 170 (PGP 170), presents in the cells over-expressing gene of drugs multiresistance (MDR1); this protein like protection pump extrudes by the cell a width range of molecules, included 99mTc MIBI. The studies have demonstrated an extremely fast washout of radiotracer by cells with high levels of PGP 170, in comparison with those to low expression. Crane et al. have studied the pattern of 99mTc MIBI biodistribution in the c-neo OncoMouse, a transgenic rat that spontaneously develops

breast cancer. The mean value of retention resulted equal to 0.38% ± 0,2% of injected dose for tissue gram, with a maximum equal to 0.94% ± 0.85% in cancer uptake.

Omar et al. have demonstrated as the premature uptake in benign and malignant lesions is correlated to angiogenesi degree, that is the growth percentage of new blood vessel induced by cancer.

Scopinaro ET al., using a particular technique to color cells, like used in blood micro-vessels counting, have studied the angiogenesi role, demonstrating as MIBI may be utilized like a invasiveness index of breast carcinoma, with a uptake correlated to level of angiogenesi and to oxidative metabolism.

Buscombe et al., finally, have demonstrated that also the histological analysis of the tumor is a determining factor for radiotracer uptake level: the ductal carcinoma, as in situ that invasive, has an elevated tumor/background activity ratio, while the papillary carcinoma, characterized by an insufficient number of cells and slow growth, often does not shows meaningful uptake.

Clinical method for scintimammography by Anger Camera

Several techniques for scintimammography by Anger Camera was introduced but the most reliable was proposed by Prof. Khalkhali: the technique consists to acquire a breast image with patient in prone position, 5-15 minutes after the injection by vein of 740 MBq (20 mCi) of ^{99m}Tc. The obtained imagine in prone position offers advantages respect to the supine one, because a better separation between cardiac and hepatic tissue emission is obtained. These organs present a high MIBI uptake, able to mask the breast tissue emission. The prone position moreover allows examining breast tissue portion next to chest. The image acquisition time is usually 10 minutes

The clinical results demonstrate an overall value of sensibility to diagnose primary breast tumor ranged by 80% to 90%. The sensibility for palpable lesions is meaningfully more high that for not palpable ones and in lesions with dimension less than 1 cm, the sensibility comes down under 50%. In literature, localization of lesions with diameter less the 5 mm by scintimammography with Anger Camera does not result. This is the main limit about application of scintimammography like principal screening technique for breast cancer.

IMI Project

Like mentioned in the previous paragraph, the scintimammography by Anger Camera sets to 1 cm the limit size for detectable tumor, highlighting the necessity to develop new mammographic and scintigraphic technologies that allow an early diagnosis of pathology. In particular about a dual modality diagnosis technique (Rx and Gamma) the finality is to implement how much possible diagnosis ability of each techniques, in terms of contrast and spatial resolution, and to realize dual modality images in order to facilitate the lesions detection.

In the last years some sections of National Institute for Nuclear Physics and Physics Departments of Italian Universities was evolved in order to arrange detectors and electronic readouts, originally developed for experiments of high energy physics, for applications in Medical Physics.

All these studies was integrated in Imaging Integrated Mammografico (IMI) project, approved by the Italian government (law 46/82 -art.10), for a term of three years; the project was finalized to new biomedical technologies development able to early diagnose breast cancer. The project, inside technological transfer activity of INFN and Italian Universities, involved five Italian industries: LABEN, CAEN, AMS, GILARDONI and POL.HI.TECH.

The aim of the project is the realization of an integrated dual modality detector for clinical application in early diagnosis of breast tumor. About functional imaging in Nuclear Medicine, the project provides the development of a high spatial resolution large FOV gamma camera that is the specific argument of this thesis. About RX imaging, more properly morphologic, the project provides the development of a prototype based on a monochromatic high intensity X ray source.

The realization of dual modality Rx and Gamma images implies the same image acquisition projection for both technique, in particular craniocaudal projection. About gamma imaging this innovation, with camera compactness, introduces the twofold advantage to reduce detector-collimator distance, and to operate breast compression, reducing therefore health tissue scattering contribution (see Figure 3I). The new conception Gamma Camera has been projected specifically in order to offer functional images with higher contrast, respect to Anger Camera ones, to detect tumor less then 0.8 mm size. To such scope, the prototype was planned in order to use recent technological innovations like scintillation crystal arrays, with pixel dimension less than 2 millimeter,

and a new generation position sensitive photomultiplier (PSPMT), that introduces a negligible contribution to intrinsic spatial resolution, utilizing metal channel dynodes technology.

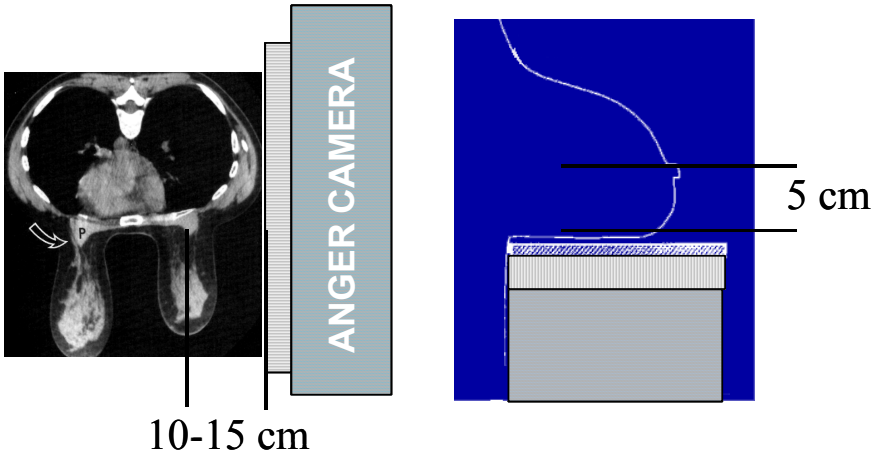

Figure 3I. Comparison between prone projection, on the left, and craniocaudal projection to right, in scintimammography

In this project a digital acquisition system for RX detector is proposed too, with a dynamic range of the order of 10^4, based on GaAs array detectors. The single detector unit is connected, by a bump bonding system, with dedicated system readout, developed by Medipix in collaboration with CERN. The detection efficiency of this unit is approximately 100% to mammography energy, allowing to reduce considerably the transferred dose to patient. The main difficulty of conventional mammography is the detection of objects with low contrast respect to healthy tissue, because of the low difference between the absorption coefficients of tissues. Different theoretical studies are concentrated on mammographic images analysis in order to determine the energy range where SNR value is higher for dose lower to the patient. Experiments with synchrotron radiation have shown that monochromatic beams in the range of 17-20 keV can be considered ideal probe for an easy location of breast lesions. The conclusion is that ideal X-ray source for mammography would have to produce low energy spectra with one tightened band tunable. Project IMI had the objective to produce this X ray source via Bragg diffraction on a crystal mosaic, using an X-ray conventional tube powered by high frequency and high voltage supply, developed by Gilardoni Laboratories. Radiographic tests have allowed comparing this source with conventional ones utilized in the mammographic systems, showing that the same quality of image is obtainable with a 50% reduced dose. The project allows realizing an instrument that will be used for clinical applications in the main Italian oncology hospitals.

Purpose of the thesis

The aim of present thesis is experimentation of new technologies and methodologies for single photon (SPE) imaging in Nuclear Medicine. In particular in breast cancer diagnosis, the activity was finalized to the realization of a Gamma Camera with high spatial resolution and large FOV, inside Integrated Mammographic Imaging project. The design of Gamma Camera prototype, in order to obtain high spatial resolution values, allows to diagnose malignant lesion less then 8 mm size. The camera is based on the most innovative technologies about position sensitive photomultipliers and scintillation crystal array. The final result is the production of a detector based on 6x7 position sensitive photomultipliers array coupled to NaI (Tl) scintillation array and the relative clinical trial in the Nuclear Medicine Department of Policlinico Umberto I in Rome

The first step of project is the realization of a medium FOV Gamma Camera prototype. On this prototype, tests about design principles validity and calibration measurements were made, in order to characterize the detector in terms of imaging.

Image reconstruction software, for the realization of image analysis console, was also developed.

In collaboration with University of Ferrara, the multivariate image analysis (MIA) was applied on the clinical images in order to improve image contrast and to better characterize suspicious lesions.

In the last 10 years, the researchers effort to realize more specific radiotracers, respect to MIBI, has been particularly consisting even if clinical experimentations are not begun still. On the contrary new imaging technologies, proposed in this thesis, may greatly contribute to new in vivo experiments in small animal imaging. In fact, in collaboration with University and Jefferson Lab. of Virginia (USA), a new prototype of gamma camera with very high spatial resolution was developed. This new detector was utilized in calibration test and finally in a small animal imaging experiment. The *in vivo* experiment represented a study of a new radiotracer dedicated to blow inflammation location (IBD), representing the second more common pathology in the world.

Experimental Method

The aim of this work was the experimentation of new technologies and methodologies for single photon imaging in Nuclear Medicine, and in particular in early diagnosis of breast cancer.

Single photon imaging is utilized in order to obtain a radiotracer bio-distribution image of patient. The more diffused SPE detector is Anger Camera; the detector is realized by a planar NaI (Tl) scintillation crystal with large area and by a traditional photomultiplier tube (PMT), array scintillation for light readout. Also the camera is equipped with a parallel hole collimator that allows to select only photons perpendicularly incidents on scintillator surface. The event position reconstruction is calculated by centroid method on photomultipliers output. The advantages of a detector like Anger Camera (shown in figure 1M) are the high detection efficiency and the good intrinsic spatial resolution value (≈ 3.7 mm), fitting the clinical necessities and spatial resolution limits due to the collimator. The disadvantage is the large detection area (≈ 50 cm diameter), that doesn't fit with dimension of specific organs, and sets a limit about the maximum counting rate, because all detection area is utilized to calculate interaction position by centroid method.

On the right in figure 1M, the pulse height distribution obtained by a total body scintigraphy with Anger Camera is shown. It is evident a phototopeak component at high energy, due to primary photons escaping from the body and subsequently interacting by photoelectric effect in scintillation crystal, and Compton component at low energy, due to primary photons interacting in the scintillation crystal via Compton effect and to photons scattered in the body and subsequently in scintillation crystal. This scattering component is obviously no useful to reconstruct image; consequently the scintigraphic image is realized only by events coming from photopeak component of energy spectra.

In figure 2M energy spectra obtained by scintimammography with Anger Camera is shown. In figure a large scattering component is visible, not well separated by photopeak ones. Consequently the Nuclear Medicine clinical protocol provides a selection of events belonging to energy spectra window equal to ±10% photopeak channel, to realize image. This windowing process therefore emphasizes the importance of a good energetic resolution in order to have high counting images.

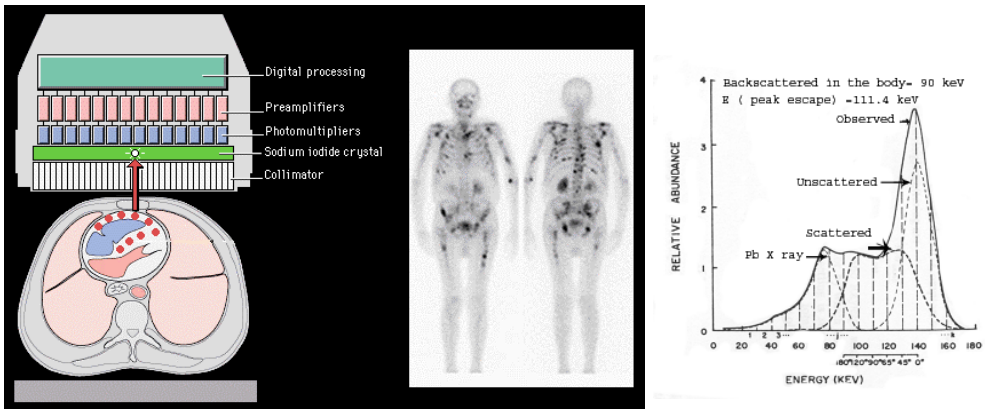

Figure 1M: Scintigraphic image by Anger Camera. From left towards right: the emitting body and the detector, a total body image, the energy spectra collected by Anger Camera

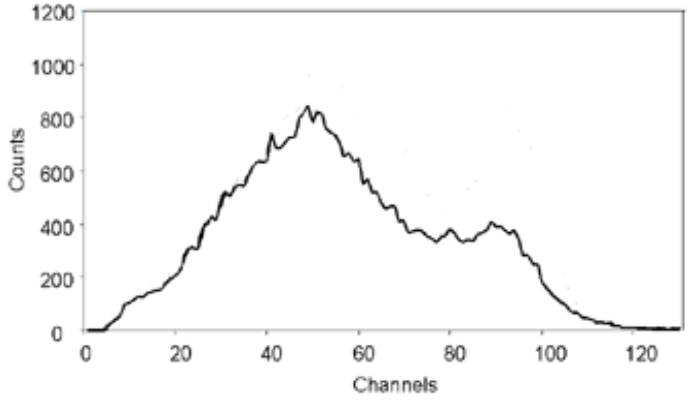

Figure 2M: Energy spectra obtained by scintimammography with Anger Camera.

In Anger Camera the spatial resolution is:

$$R = \sqrt{R_i^2 + R_c^2}$$

where Ri represents the intrinsic spatial resolution of photomultiplier+scintillator system, while the Rc represents the geometric factor by a parallel hole collimator:

$$R_c = \frac{d(L+z)}{L}$$

where d represents the hole diameter, L and z the length and the object-collimator distance respectively.

To explain the elements involved in intrinsic spatial resolution, it is necessary to better describe the SPE imaging.

Single Photon Emission Imaging

Detector Response Function

The spatial distribution function of light coming from photons interaction in scintillator crystal is named PSF (Point Spread Function). Considering the light principally due to primary photoelectric interactions, the spatial distribution will be a quadratic bi-dimensional function, representing the projection, on detection plane, of solid angle of photons acceptance. The light distribution is sampled by photomultipliers array and the even position is computed by centroid algorithm on photomultiplier outputs.

The detector charge distribution doesn't coincide with PSF, because of the dimensions and the no-homogeneity gain of photodetector.

In order to represent analytically the light sampling, the detector response function (Detector Response Function - DRF) is introduced:

$$DRF = DRF(r,z) = \int P(x,y)PSF\left\{\left[(x-r)^2 + y^2\right]^{1/2}, z\right\}dxdy$$

where P(x, y) is the quantum efficiency of single sampler, PSF(r, z) is the distribution of incident light, z the depth of interaction respect to the photomultiplier level and r the distance, on the photomultiplier level, between light centroid position and photocathode center. In figure 3M the formation of a radiographic image through reinforced screen, typically scintillator material, is shown, in function of the event-photodetector distance. Even if it is not a scintigraphic image, the figure allows visualizing the DRF concept like a function of z, that is the interaction point in the scintillator to photodetector level distance. The event detected to greater distance from photodetector level produces a larger distribution respect to the deepest one.

The DRF equation, defining opportunely P(x, y) function, may be applied to various systems that utilize centroid method, and in particular in Anger Camera is:

$$DRF = n_{fe}(r,z)$$

DRF represents therefore number of photoelectrons produced by photocathode for all events, in function of the interaction distance r and depth z. After multiplication charge process in PMT, DRF corresponds to total collected charge on anode. Therefore the scintillation light distribution is reconstructed measuring charge collected by

photomultiplier, taking into account the response homogeneity, the dead zones and the number of PMTs.

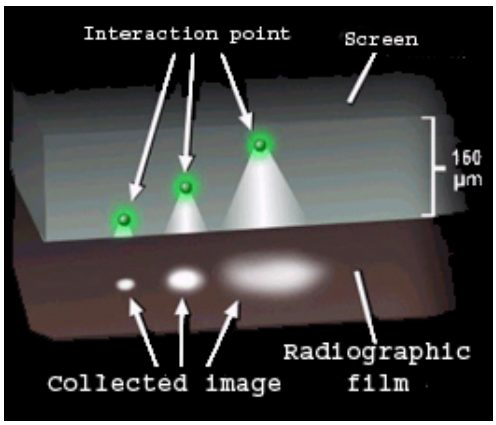

Figure 3M: Radiographic image with reinforce screen, typically scintillator crystal, in function of the distance of the event from the photodetector, in this case radiographic film

Intrinsic spatial resolution strongly depends on statistical error due to determination of DRF distribution center, and can be estimated by:

$$\sigma_x = \frac{\sigma_{DRF}}{\sqrt{N}}$$

where σ_{DRF} is the standard deviation of the single measured values n^i_{fe} [where i = i(r,z)] and n indicates the total photoelectrons number.

Consequently, the intrinsic spatial resolution coincides with standard deviation of measured values mean. In particular, if a n^i_{fe} population greater than i is used, the standard deviation σ_{DRF} would not change appreciably. On the contrary, the standard deviation of the mean σx, improves slowly when N increases. Practically, to improve intrinsic spatial resolution it is necessary to improve standard deviation σ_{DRF}, that is to reduce the FWHM of light distribution produced by scintillator. From considerations on spatial and energy resolution it is possible to write:

$$RS = \frac{PSF_{drf}}{\sqrt{N_{fe}}}$$

fundamental relation for every system applying centroid algorithm.

Event position by centroid algorithm

The algorithm commonly utilized to calculate scintillation event position is centroid method on detector outputs x_i. The X signal is a function of z_i outputs of PMT sampling the light distribution coming from crystal:

$$X = X(z_1, z_2, ...z_N)$$

For Anger Camera:

$$X(z_1, z_2, ...z_N) = X(Gn_1, Gn_2, ...Gn_N)$$

where the gain of different elements is considered equal to G and n_i is the number of photoelectrons impinging on first PMT dinode. So it is obvious that the n_i values depend on interaction coordinates (x,y).

Considering n_i value changing in agreement to Poisson statistics, the standard deviation of X is:

$$\sigma = \left\{\sum_i k_i^2 G^2 n_i\right\}^{\frac{1}{2}} \quad \text{where} \quad k_i = \frac{\partial X}{\partial z_i}$$

and ki is the contribute of PMT_i to the X signal. The position sensibility S is:

$$S = \frac{dX}{dx} = \sum_i k_i G \frac{dn_i}{dx}$$

So the spatial resolution, normalized to the sensibility value, in terms of standard deviation, is:

$$R = \frac{\sigma}{S} = \frac{\left\{\sum_i k_i^2 G^2 n_i\right\}^{\frac{1}{2}}}{\sum_i k_i \frac{dn_i}{dx}}$$

The k_i coefficients are determined by minimum value of R, that is such that $\frac{\partial R}{\partial k_i} = 0$

$$k_i = \frac{\left\{\sum_i k_i^2 n_i\right\}}{\sum_i k_i \frac{dn_i}{dx}} \cdot \frac{1}{n_i} \cdot \frac{dn_i}{dx} = \frac{R^2 S}{G} \frac{dn_i}{dx} \frac{1}{n_i}$$

The {ki} set is defined less than a constant value, and replacing R formula we obtain Rmin:

$$R_{\min} = \frac{1}{\sqrt{\left\{\sum_i \frac{1}{n_i} \cdot \left(\frac{dn_i}{dx}\right)^2\right\}}}$$

This Rmin value is function of scintillation coordinates (x,y) and represents the theoretical minimal limit for spatial resolution of a detector applying centroid algorithm to calculate radiation interaction position. Moreover supposing response sensibility S like a constant value, we obtain:

$$k_i = CR_{\min}^2 \frac{dn_i}{dx} \frac{1}{n_i} \text{ with C =constant}$$

Charge distribution sampling

A detector that applies centroid algorithm to determine the interaction position is strictly related to scintillation light sampling. In figure 4M, DRF vs. interaction point distance is shown, where the photomultipliers involved in light sampling are indicated.

The figure shows that in sampling of a typical Anger Camera PSF, approximately 8 cm FWHM, seven photomultiplier, 5 cm diameter, are involved. Since every sampling operation depends on Shannon theorem, it is clear that if the light distribution FWHM is comparable to sampler dimensions, that is the photomultiplier diameter, a sampling error occurs degrading the detector intrinsic spatial resolution.

The photodetector dimension, in agreement with scintillation light distribution, therefore influences the final performances of detector. An accurate sampling improves the sensibility of centroid determination but at the same time reduces the fraction of charge collected by sampler, introducing a limit due to the noise of each element.

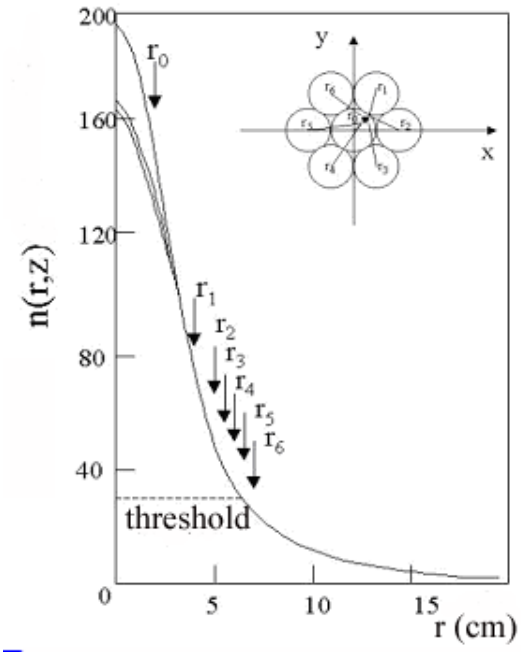

Figure 4M: DRF vs the distance by the interaction point (origin of abscissa) is shown, where the photomultipliers involved in the light sampling are indicated.

From the previous considerations, it is possible to conclude that it is no easy to increase the performances of current Anger Cameras, already optimized by reducing the planar crystal thickness (in order to minimize the PSF FWHM) and utilizing hexagonal photomultiplier (in order to reduce the dead zone due to the multiple assembly). So at moment the superior limit of intrinsic spatial resolution for this detector is 3.5 mm.

New technology for SPE imaging

The aim to develop new detectors dedicated to SPE is to detect small objects, in particular in scintimammography with dimension less than 0.5 cm. Skipping for the moment the spatial resolution component due to the collimator, in order to improve the intrinsic spatial resolution of a gamma camera, we have to act directly on photomultiplier-scintillator system response. In this class of detectors it is important to distinguish between two different PSF:

1) a light PSF, that is the light distribution coming from a scintillation event.

2) an image PSF defined as distribution function of the events on the detector coming from a point source.

In figure 5M, the left part shows the light distribution inside a planar scintillation crystal, where many reflection events occurred. Recently scintillation crystal array are available, where the crystal is composed by independent elements, optically isolated like shown in the right part of figure 5M. Due to mechanical problems, initially only materials as the YAP and the CsI(Tl) were utilized to realize scintillation array; these scintillation material present a reduced light output respect to the NaI(Tl) scintillation, to the detriment of energy resolution. Fortunately in last the 5 years NaI(Tl) scintillation array was developed with pixel up to 1 mm^2size.

The single pixel operates like a guide for scintillation light; so light PSF coming from crystal presents an FWHM equal to pixel size. Since NaI(Tl) is a hygroscopic material, to package the crystal a glass window is introduced, so increasing light PSF.

Other advantage introduced by scintillation array is the intrinsic position linearity. In figure 6M the position linearity for a planar crystal and a scintillation array are shown. The data are obtained scanning detector surface with a point source, at fixed step. On x axis we report the source mechanical position on detector, while on the y-axis the spot position measured in the image. The figure 6M shows clearly that the planar crystal response presents a spatial no-linearity in the crystal peripheral zone, due to a cutting off in light sampling by photomultipliers. On the contrary, for crystal array the position response is more linear due to geometrical restraint operated by single crystal on scintillation light.

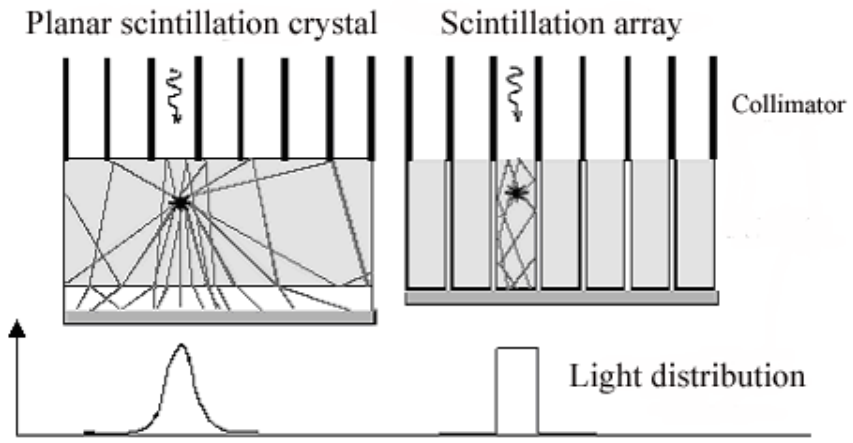

Figure 5M: Light distribution obtained by a planar, on the left, and by a scintillation array, on the right

In term of image PSF, a technological innovation like position sensitive photomultipliers (PSPMTs) allows to exceed the limits imposed on image reconstruction by centroid algorithm and to resolve the problem about dead zone between PMTs. The traditional photomultipliers have a cathode that transforms the incident light in photoelectrons, in function of photocathode efficiency. The electrons are multiplied by dinodes grid and subsequently collected by an anode, producing an output current proportional to primary energy photon

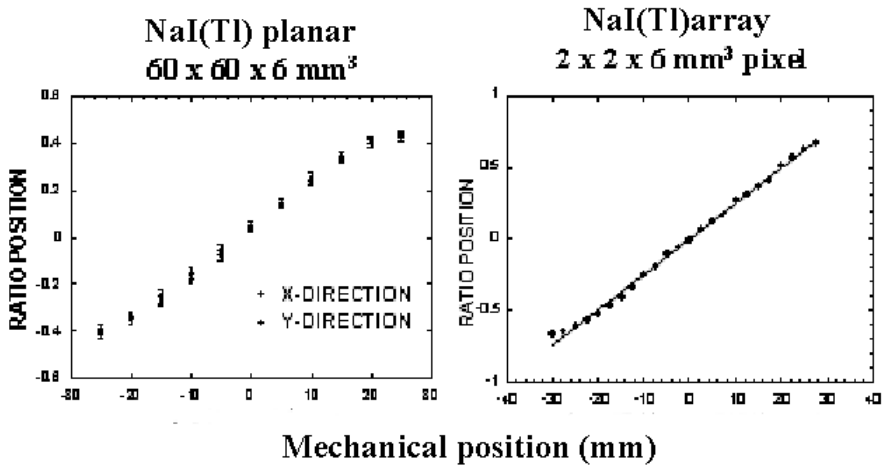

Figure 6M: Position linearity of a planar crystal, on the left, and of a crystal array, on the right

The PSPMT is an independent imaging system where the anodic plane is realized by single elements (wires or pitchs) sampling the charge in two directions, X and Y. By centroid method applied to single anodic charge, it is possible to reconstruct the event coordinates (see. Figure 7M). Consequently, replacing in a gamma camera standard photomultipliers array with a position sensitive photomultiplier, it is possible to improve the light sampling and to reduce the electronic noise.

The dinodes grid introduces a cathode charge spread and consequently it contributes to PSF FWHM and therefore to spatial resolution deterioration (see Fig. 7M). The last technological innovation about PSPMTs has allowed to realize a new system of electrons multiplication by metal channel that reduces the charge spread introduced by PMT less than 0.5 mm FWHM, like shown in figure 8M.

The metal channel system is realized by an array of linear focusing dinodes where only the dinodes closer to secondary electrons path are involved. So using metal channel PSPMT it is possible to directly measure the scintillation crystal PSF, neglecting charge spread due to PMT.

The housing of metal channel structure (fraction of millimeter) allows an evolution about dimensioning and assembling of gamma camera detectors, in particular in array configuration: substituting the round shape with a square ones, with compact size, it is possible to reduce glass window (from 6 to 3 mm), and to increase active area/total area ratio, from 57% to 70%.

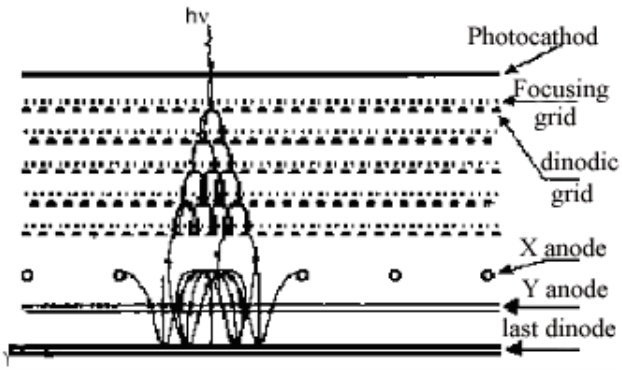

Figure 7M: Focusing mesh of the dinodic structure in first generation of Hamamatsu PSPMT. Example of charge distribution by a scintillation event.

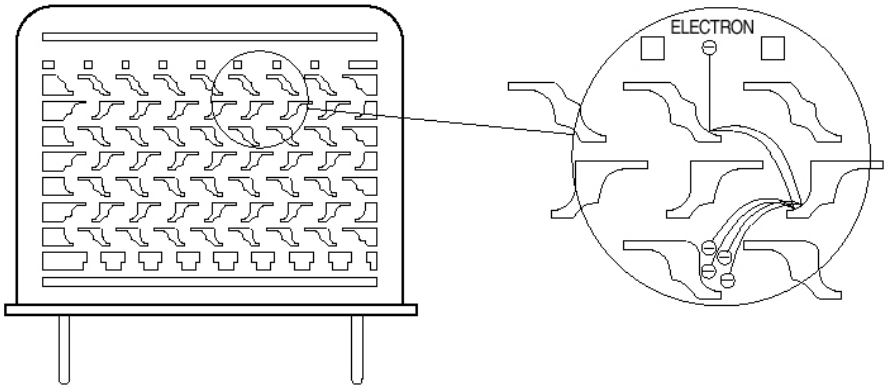

Figure 8M Process of charge multiplication in a metal channel PSPMT and anodic structure.

Image correction (LUT)

The figure 9M shows a gamma ray image obtained by a 4x4 PSPMT array coupled optically to a NaI(Tl) scintillation array, like the medium FOV Gamma Camera prototype developed inside IMI Project. The image is pixellated because results by superposition of the images coming from each pixel. So the image represents a image PSF of each single element and we can considered this detector like a matrix of independent detectors, that is the single crystal pixel.

In figure 9M the image shows position distortions and counting no-homogeneity; such distortions are due to gain differences of photomultipliers, to different light output by each crystal pixel, to errors on scintillation light sampling in the single tubes edges, to geometric effect of collimator pattern on the crystal array ones and to the reduction of detection efficiency in the dead zone between PSPMTs.

Like for all composed detectors, the image correction process, "look up table" - LUT, is introduced, based on the localization of events coming from each detector element, that is the determination of spatial coordinates and energy value for each event belonging to each single detector. Obviously this procedure depends strongly by visual single pixel identification that still depends on optimization of light collection and on spatial resolution. The first step of procedure consists in redistributing the events of single pixel in a regular matrix, reproducing crystal physical structure, defining a spatial grid of spatial events selection, like shown in the right on figure 9M.

The second step regards the alignment of the photopeak channel by each single pixel energy spectra, in order to obtain a gain equalization (gain correction). The gain correction factors are calculating by the ratio between the overall energy spectra and single pixel center of gravity. The final result is a gain correction that improves the energy resolution, allowing a better definition of energy windowing to select photopeak events for imaging. In figure 10M the effect of this energy spectra correction is shown for medium FOV gamma camera.

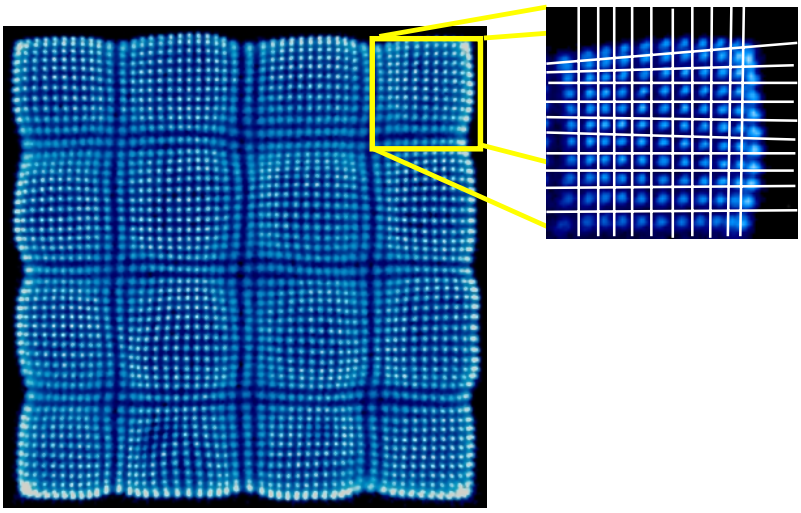

Figure 9M: Position grid to identify the events coming from each single pixel

The energetic resolution is approximately 16% @140 keV and the photofraction, photopeak / overall energy spectra counting ratio, is 73%. This optimization of energy spectra and therefore of detector energetic resolution permits to extend the range of events acceptance for imaging to the right photopeak half section.

The last step of the correction consists in summing the events inside each pixel crystal belonging to defined energy window. A new array of coefficients is generated to obtain counting homogeneity of image (counting homogeneity).

The final result is a reconstructed image with a elements number equal to pixel crystal number of scintillation array, shown in figure 11M left side, where counting homogeneity is ≤ 5%.

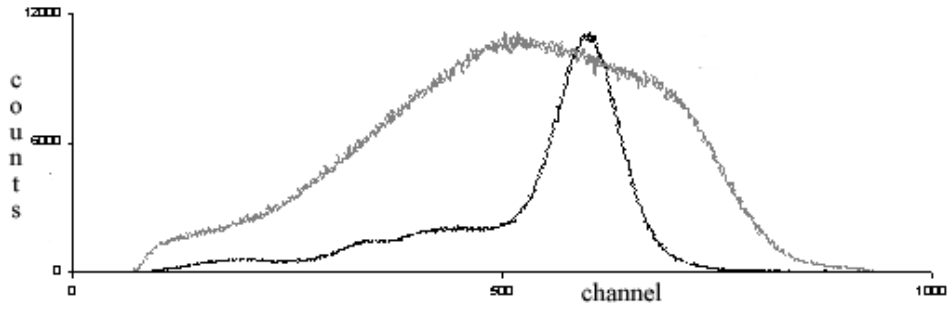

Figure 10M Energy spectra obtained by flood field irradiation with 57Co source (Eγ=122 keV). 4x4 PSPMT gamma camera prototype. In gray the original energy spectra and in black the spectra after the gain correction procedure

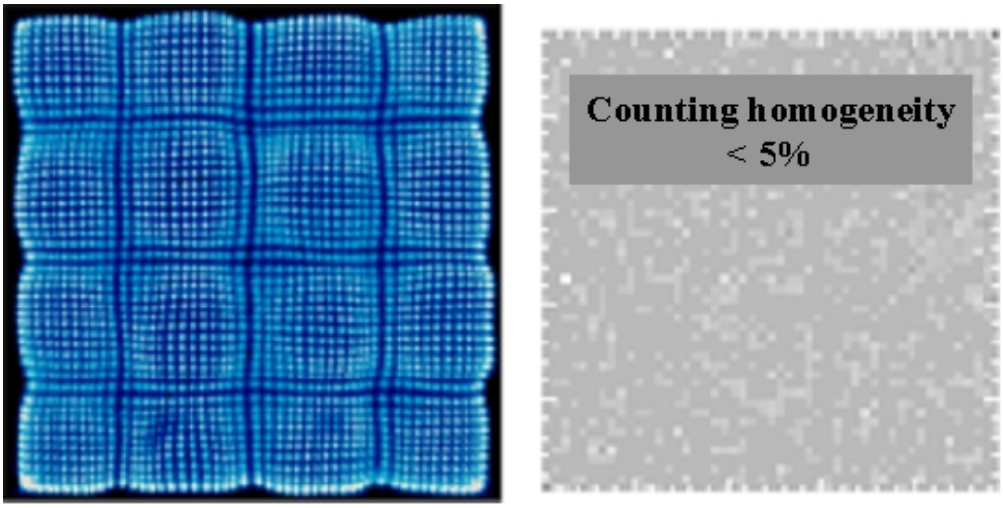

Figure 11M Raw Image and reconstructed image after LUT. procedure.

Multivariate image analysis (MIA) on scintimammography images

Multivariate Image as three-way array

The multivariate image **G** is a three-way data array, a stack of congruent images, with each two-way image in the stack measured for a different 'variable'; i.e., the energy windows. A digitized image is a matrix **G** of data of indices I, J. When many variable are involved, an index K is added to make **G** a three-way array **G** of indices I, J, K, and elements, $g_{i,j,k}$ If the geometry in the image is temporarily ignored the three-way array **G** of dimension IxJxK can be reorganized in a two-way array **X** of dimension (IxJ)xK, with the K energy windows as 'variable'. Matrix **X** allows the use of Principal Component Analysis (PCA) for data analysis in the variable space. PCA results on multivariate image can show visually.

Principal Component Analysis

Given a matrix **X**(NxK) where the K columns are variables and the N rows observations, PCA is the decomposition of a matrix **X** into simpler matrix $\mathbf{M}_a$:

$$\mathbf{X} = \sum_{a=1}^{A} \mathbf{M}_a \qquad (1)$$

The smallest value of A for which this equation still works is called the *rank* of **X**. The $\mathbf{M}_a$ are matrices of size NxK and have *rank*=1. They can therefore be represented as outer products of two vectors, **t** and **p**:

$$\mathbf{M}_a = \mathbf{t}_a \mathbf{p}_a^T \qquad (2)$$

The $\mathbf{t}_a$ are vectors of size Nx1 and the $\mathbf{p}_a$ are vectors of size Kx1. The total PCA equation becomes:

$$\mathbf{X} = \sum_{a=1}^{A} \mathbf{M}_a = \sum_{a=1}^{A} \mathbf{t}_a \mathbf{p}_a^T \qquad (3)$$

Vectors $\mathbf{t}_a$ are called *scores vectors* and the vectors $\mathbf{p}_a$ are called *loadings vectors*. The loadings vectors have the property o orthonormality $\mathbf{p}_i{}^T\mathbf{p}_j=\delta_{ij}$ and are the eigenvector of $\mathbf{X}^T\mathbf{X}$. The scores vectors have the property of orthogonality $\mathbf{t}_i{}^T\mathbf{t}_j=\delta_{ij}\lambda_i$ where λ_i is an eigenvalue of $\mathbf{X}^T\mathbf{X}$.

Equation 3 for A=K exactly reproduces the elements $g_{i,j,k}$ of the stack of images $\underline{\mathbf{G}}$. These images are the column vectors of matrix **X** and the single images **G** can be obtained by a simple vector to matrix reorganization.

Application on Scintimammography images

The goal of multivariate image analysis (MIA) is to extract significant information from an image data set while reducing the dimensionality of the data. The MIA makes use of the Principal Component Analysis (PCA). The possibility to consider the spectrum resulting from the imager as set of images is evident in Fig.12MA). Extending the conventional approach based on the 'photopeak' energy window, the total pulse height distribution was described by six energy windows called w1 to w6. To this respect, the output of the imager can be considered as a stack of images each of them viewing the same field-of-view; i.e., a multivariate image PCA divides information into orthogonal components by transforming multivariate images into a number of principal component (also called scores) images that carry information related to these orthogonal components. The first principal component (factor) account for as much of the variability as possible, and has the largest eigenvalue, l, associated with it and each succeeding factors account for as much of the remaining variability as possible. The primary components are those corresponding to the largest eigenvalues and represent the set of factors that are required to reproduce the original data-set within the experimental error. The remaining principal components, each describing a low variance, represent noise. The idea behind MIA is presented in Fig.12MB.

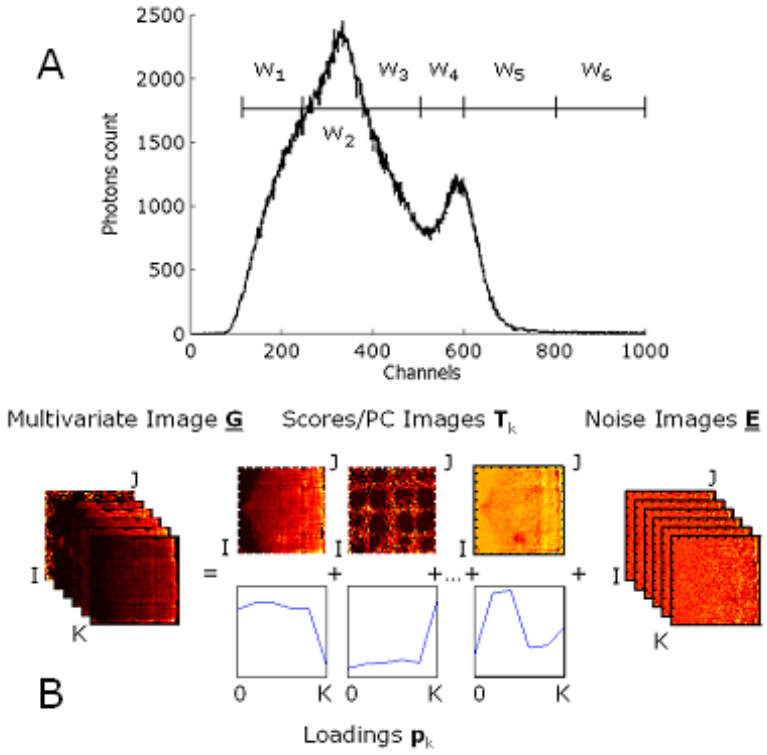

Figure 12m: A) Detector pulse height distribution with the photopeak and energy windows. B) Multivariate Image Analysis algorithm. The series of K images is decomposed via Principal Component image analysis into K principal components images (scores images) and loadings associated with each of them. The A components represent significant variation within the original variables K, whereas (K-A) represent noise in the original variables and are included into error images E.

The objective is to identify images that are globally correlated or anticorrelated. This information can be displayed as loadings of the different image variables; whereas the pixels that are responsible for the correlation can be displayed as scores images. Score image may be easier to interpret than the variable images. With reference to Scintimammographic imaging, Multivariate Image Analysis is a data reduction and information retrieval technique that identifies the Tc^{99m} emitted photons and Compton scattering present in the windowed spectra of Fig.12MA), and collects them as separated images.

New frontiers in small animal imaging

Like emphasized previously, the aim of this thesis is the experimentation of new technologies and methodologies for single photon (SPE) imaging. Coherently with this philosophy, the performances of a gamma camera prototype were tested, based on the most recent innovations in terms of mechanical assembling, realized in collaboration with Physics Department of Jefferson Laboratory, Newport News, Va.USA. The gamma

ray imaging is utilized, besides for cancer diagnosis, *in vivo* experiment to test radiotracers dedicated to genetic transcription and proteins expression. Iodio125 is the radioisotope mainly used with molecules like nucleic acids and antibodies in biological experiment and its long half life (60,2 days) is particularly useful in small animal imaging. The ideal detector in Nuclear Medicine would have to be projected in order to obtain a compromise between spatial resolution, detection sensibility, detection area and realization cost. Unfortunately ^{125}I low emission energy doesn't permit to satisfy both necessities of high spatial resolution and large detection area; furthermore the low dose administered to small animals, associated with high spatial resolution collimators, prevents formation of useful images.

Detectors bases on scintillator array, introduced in this thesis, present a reduction of scintillation efficiency due to dead area, necessary to guarantee the optical isolation between each crystal pixel. Moreover I^{125} low emission energy (27 keV) involves a low light output by scintillator, and therefore a reduction of pixel identification ability of detector, with consequent decreasing of spatial resolution and image contrast.

In order to obviate these disadvantages, it is necessary to use a planar crystal, going back to Anger Camera philosophy. But a planar crystal presents a PSF FWHM larger respect to scintillation array ones and the glass window, due to crystal hygroscopicity, increases PSF FHWM and therefore gets worse spatial resolution. Fortunately the new technology about crystal-PMT assembling allows an optically coupling of a thinnest planar crystal (1.5mm) directly on a PSPMT photocathode window (integral assembling), obviating to protection glass window, like it is shown in figure 13M.

Moreover utilizing a single position sensitive photomultiplier, it is possible to solve also the problem about dead zone between photomultipliers in an array configuration.

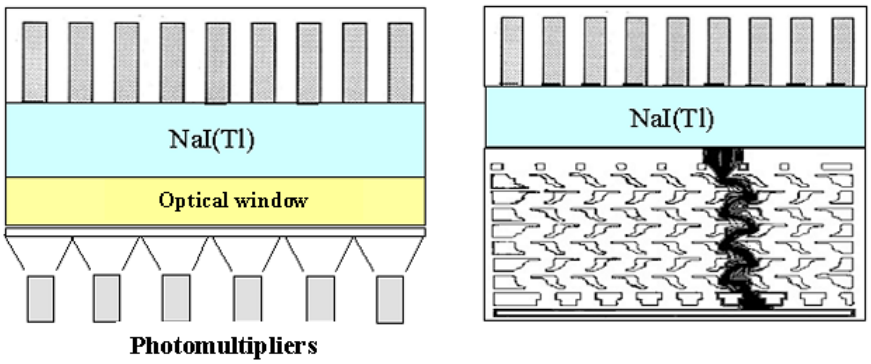

Figure 13M. On the left, the operation outline of an Anger Camera is shown. On the right instead the principle of operation of the new detector is shown

Experimental Equipment

Prototype of medium FOV high resolution gamma camera

The Imaging Integrated Mammografico project provided for first step the realization of a medium FOV gamma camera in order to test design validity and to perform preliminary clinical tests. The prototype presents a 4x4 PSPMTs R8520-00-C12 Hamamatsu array coupled to NaI(Tl) array. Each PSPMT is connected to a single resistive chain and to a single electronic readout board; so each detection module is independent by the other one. The electronic readout system was realized by CAEN industry.

R8520-00-C12 PSPMTs was developed by Hamamatsu in order to improvePSPMT spatial resolution. It has 11 metallic channels dinodic stages and 12 anodes wires, 6 for each direction (X and Y). The external area is 25.7mm^2 with 20 mm thickness, while active area is 22 mm^2

Respect to the previous version of this photomultiplier, in order to decrease the distribution light width, glass window was reduced, by 1.3 mm to 0.8 mm. Moreover, the inter-space between anodic wires was reduced in order to improve spatial linearity in edge zones, and the number of anodes was increased by 4 to 6.

The flange removal on bottom of metallic structure active/overall area ratio was increased by 63% to 73%, in order to create PMTs compact array, reducing peripheral dead zone.

The NaI(Tl) scintillator array was produced by Saint Gobain, with 1.8x1.8x6mm^3 pixel size (2x2 mm^2 pitch); the overall dimension was 106x106 mm^2 (active area 99.8x99.8 mm^2). The scintillator thickness was 12 mm, including 3mm glass window and 3 mm aluminum envelope (see figure 1AS).

In figure 2AS three technical sketches of detector are shown. A General Purpose collimator, with 1.5mm hexagonal holes, 0.2mm septa and 22mm thickness, like that one used in Anger Camera, has equipped the camera.

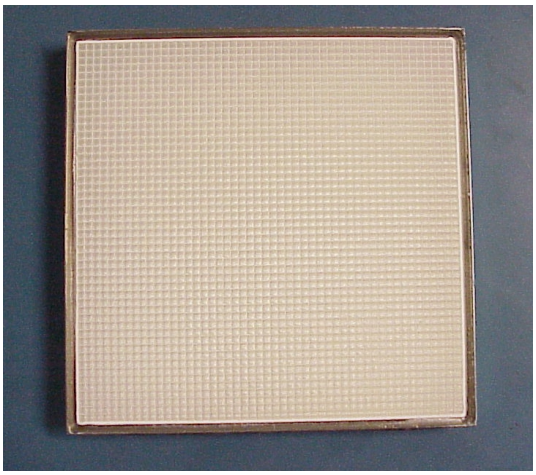

Figure 1AS 50x 50 pixel NaI(Tl) array

In figure 3AS 4x4 gamma camera pictures are shown. In addition the assembling system and lead shielding were planned with a support structure in order to integrate gamma camera on a mechanical arm that allows the acquisition of scintimammographic images in cranio-caudal projection like in mammography. For the same reason, the mechanical system has been equipped of an appropriate device for breast compression.

In figure 4AS a picture of total scintimammographic system is shown; for 4x4 PMT camera the total weight is 10 kg.

The position reconstruction algorithm is based on centroid method, where the weighted mean value, in order to calculate the X and Y coordinates, takes into account the contributions of all photomultipliers:

$$X = \frac{\sum_{i=1}^{16} x_i E_i}{\sum_{i=1}^{16} E_i} \qquad Y = \frac{\sum_{i=1}^{16} y_i E_i}{\sum_{i=1}^{16} E_i}$$

$$E_{tot} = \sum_{i=1}^{16} E_i$$

The electronic readout is realized by 16 independent elements managed by a National Instrument interface Pc board for data elaboration. The acquisition cards are assembled like shown in figure 5AS.

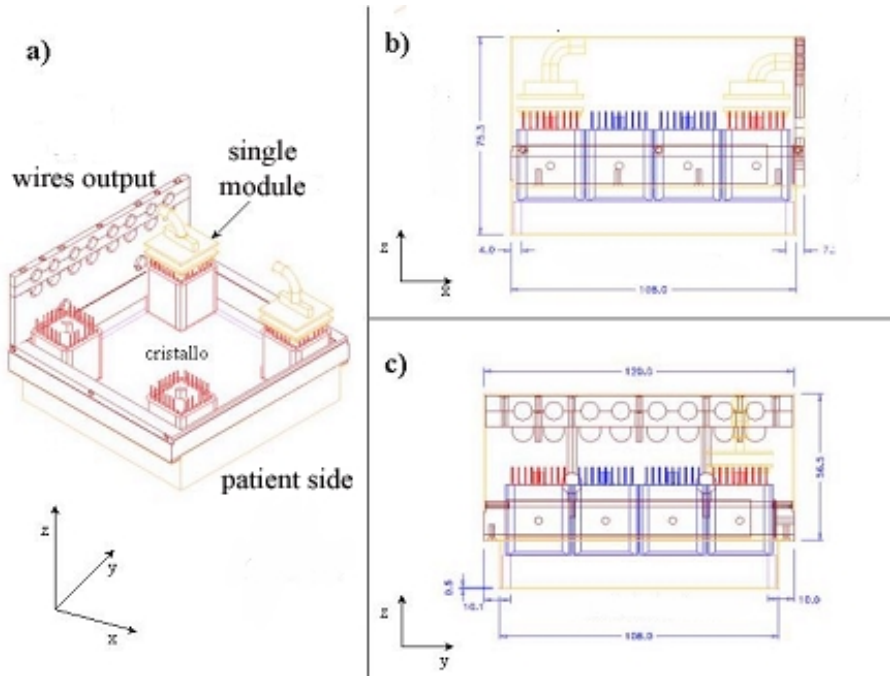

Figure 2AS Technical sketches of the 16 PSPMTs prototype in different projection

Figure 3AS 16 PSPMTs prototype pictures. a) Without scintillation crystal b) Projection of the wide side c) Overall system.

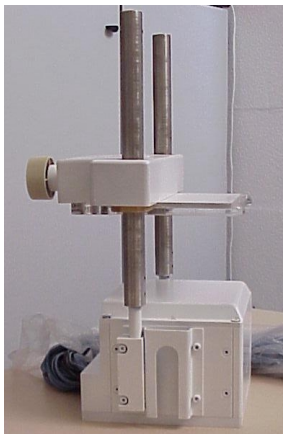

Figure 4AS 16PSPMTs camera with breast compressor

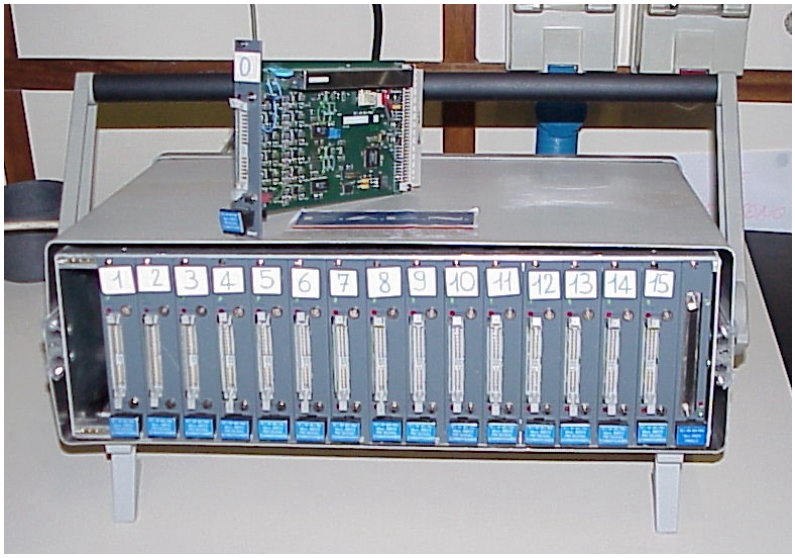

Figure 5AS Electronic readout system by C.A.E.N.

Prototype of large FOV high resolution gamma camera

The large FOV camera is based on the same realization principles of 4x4 PSPMT prototype introduced in the previous paragraph. In this case the detector is realized by 6x7 R8520-00-C12 Hamamatsu PSPMTs array coupled to a NaI(Tl) scintillation array. As in previous case, the photomultipliers are equipped by an independent electronic readout. Due to the large number of PSPMTs, the electronic readout system has been miniaturized and organized in a sandwich structure in order to reduce detector dimension (see figure 6AS). Each photomultiplier has four identical outputs (Xl, Xr, Yl, Yr) for the positioning, whose sum generates a trigger signal with amplitude proportional to the collected energy by scintillation event. This trigger signal is utilized to determine the photomultipliers involved in detected scintillation event and to reconstruct event position.

The algorithm of event position reconstruction utilizes the calculation of local coordinates of each involved photomultiplier by:

$$X_i^* = \frac{X_i^l - X_i^r}{X_i^l + X_i^r} \qquad Y_i^* = \frac{Y_i^l - Y_i^r}{Y_i^l + Y_i^r}$$

and relative energy:

$$E_i^* = X_i^l + X_i^r + Y_i^l + Y_i^r$$

Local coordinates of all involved photomultipliers define the final coordinates by:

$$X^* = \frac{\sum_i X_i^* E_i^*}{\sum_i E_i^*} \qquad Y^* = \frac{\sum_i Y_i^* E_i^*}{\sum_i E_i^*}$$

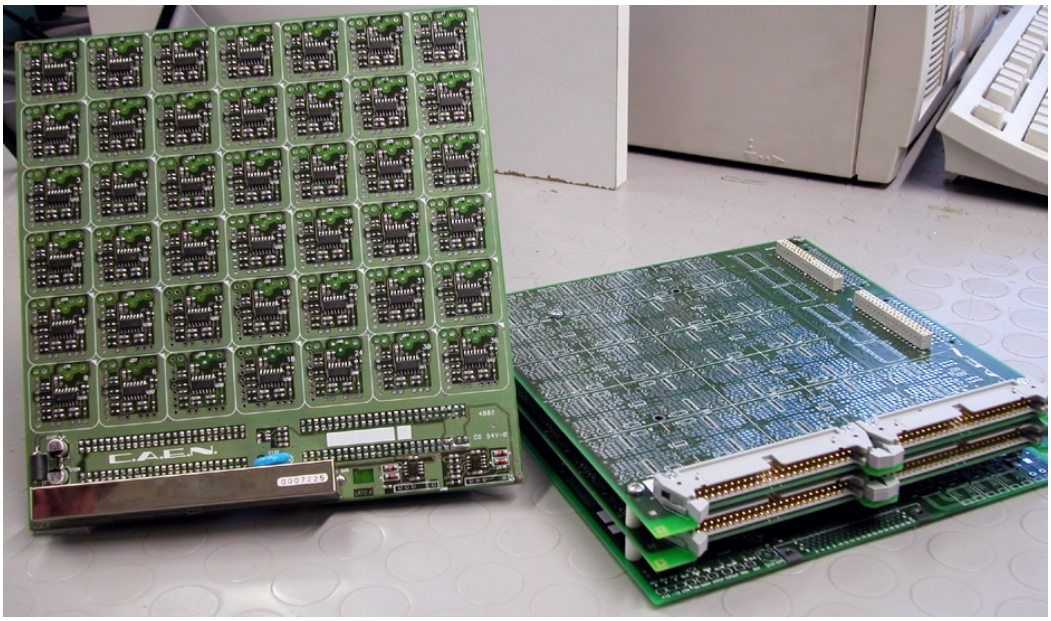

Figure 6AS: 42 PSPMT prototype electronic readout.

About the scintillator array NaI(Tl) array, the pixel size is 1,8x1,8mm^2, 2x2 mm^2 pitch. The overall dimensions are 167.2x193.1 mm^2 with 165.6x191.6 mm^2 active area. The total thickness is 12 mm, including 3mm glass window, 6mm crystal thickness and the aluminum housing. An image of the scintillator array is shown in figure 7AS.

A mechanical structure was realized in order to aligning and containing photomultipliers, minimizing dead area between PSPMTs, to guarantee the optimization of the camera side in contact with patient body and the compactness and stability. Also

this camera was equipped with a breast compression system. An image of the camera is shown in figure 8AS and figure 9AS

Figure 7AS: NaI(Tl) scintillation array

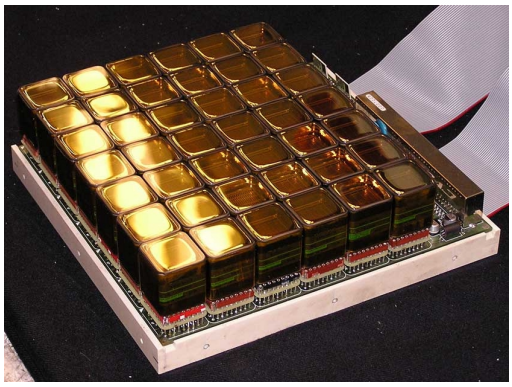

Figure 8AS 42 PSPMT camera without scintillation array

Figure 9AS 6x7 PSPMTs large FOV prototype

Very high spatial resolution gamma camera prototype, integral assembly

The detector consists on a Hamamatsu H8500 Flat panel PMT coupled in a integral assembly to a planar NaI(Tl) scintillator. The flat panel PSPMT is based on the metal channel technology and presents very compact size: the external dimensions are 51.7 mm x 51.7 mm x 15.4 mm for an active area of 49.7 x 49.7 mm2. The photocathode is bialkali, with 1.8 mm glass window, and 12 stages of dynode are used as electron multiplier. Anodic structure consists of 8x8 matrix in which each individual anode has a 6 mm side; anode gain variation was a factor of 2. The planar NaI(Tl) integral assembly was realized by Bicron solving mechanical difficulties arisen from thin photocathode glass window and crystal thickness and from hermetically sealing of the detector. The crystal has 50 x 50 mm2 size with all surface polished with white and black reflector on the back and lateral side respectively. The detector thickness is 1.5 mm allowing a

detection efficiency of 25%@140 keV. The basic detector principle is the same of an Anger camera with scaled dimensions. The sketch and the picture of detector are shown in Figure 10AS and Figure 11AS respectively.

A 64 channel 'multi-anode' read out technique was utilized for this flat panel camera, in which the charge on each anode is individually read out and digitized. The serial output is subsequently read by a 5 MHz National Instruments 6110E Analogue to Digital Converter PC board. The position is calculated directly via software utilizing the centroid algorithm. Multianode readout allows us to study how the charge is distributed on the single anode to quantify the sampling quality and to improve spatial resolution by applying special algorithm of reconstruction image like a Gauss2D fit on charge distribution.

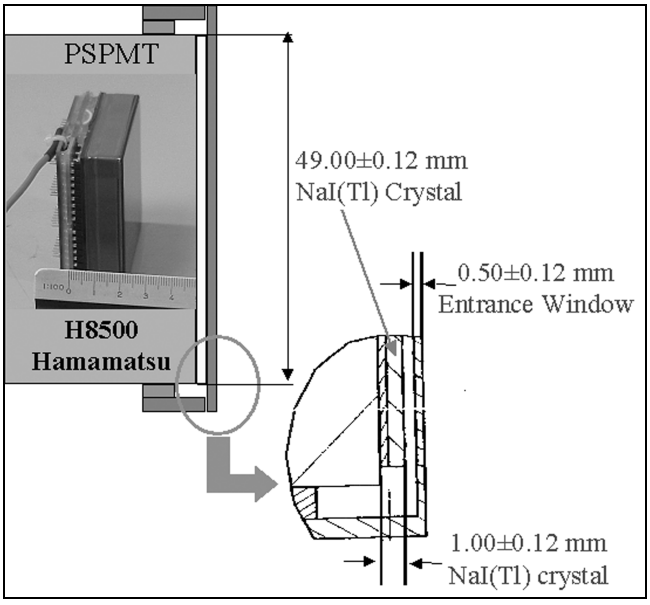

Figure 10AS: Sketch of: NaI(Tl) integral assembly detector.

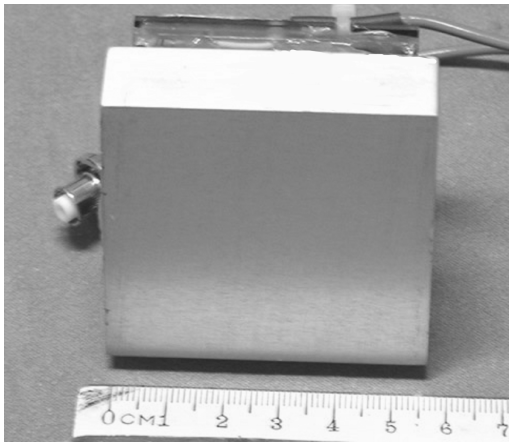

Figure 11AS: NaI(Tl) integral assembly detector.

Results

Calibration Measurements

Prototype of medium FOV high resolution gamma camera

Gain calibration of the PSPMTs

Like described, previously, each photomultiplier is equipped by a single electronic readout. Due to the variation of each response, the first step of calibration was to obtain the same energy gain for each element, acting on single high voltage, using by reference the photopeak channel in energy spectra. After the regulation, the photopeak channel for all photodetector ranged inside 5%.

Image reconstruction

A flood field irradiation of camera was operated utilizing 57Co source. In figure 1R the images obtained by single photomultiplier are shown, while in figure 2R the reconstructed image by centroid algorithm in shown. In figure 3R the image profile is shown, demonstrating that the detector allows a total recovery of scintillation events in dead zones between photomultipliers, attesting the optimal qualities of camera response

Position linearity

In order to estimate the position linearity, a 1 mm Co57point source was utilized to scan detector surface. In figure 4R the position linearity is shown, for 2 mm step. The camera presents optimal position linearity, guaranteed principally by array structure of scintillation crystal.

Energy resolution

Using the previous detector scanning measurement the energy resolution was studied, in function of source position. The result is shown in Figure 5R, where the two curves represent energy resolution in dead zone and in active zone of detector. The mean value was attested around to 20% (dead zone) and to 15% (active area), like reassumed in Table 1R.

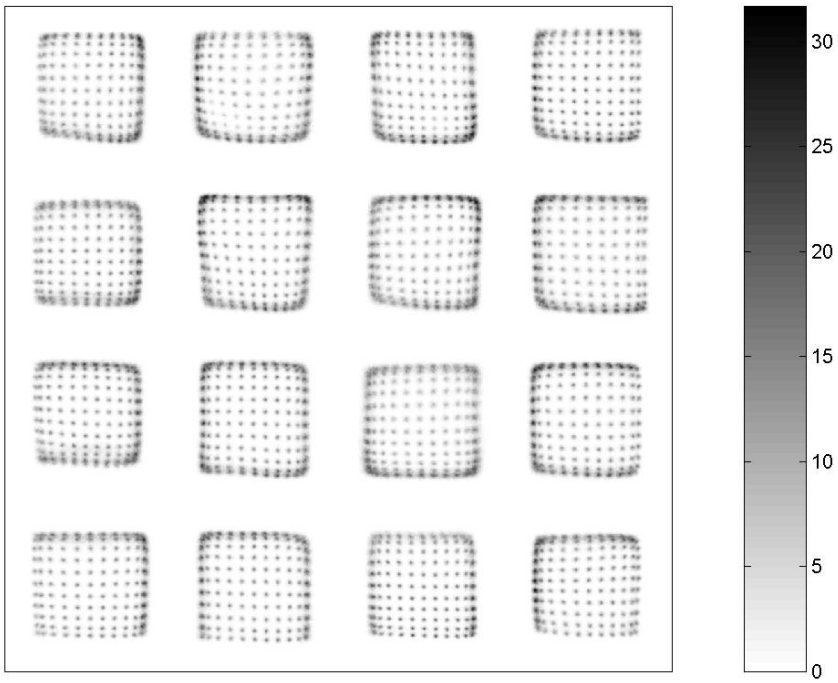

Figure 1R Images of each single photomultiplier.

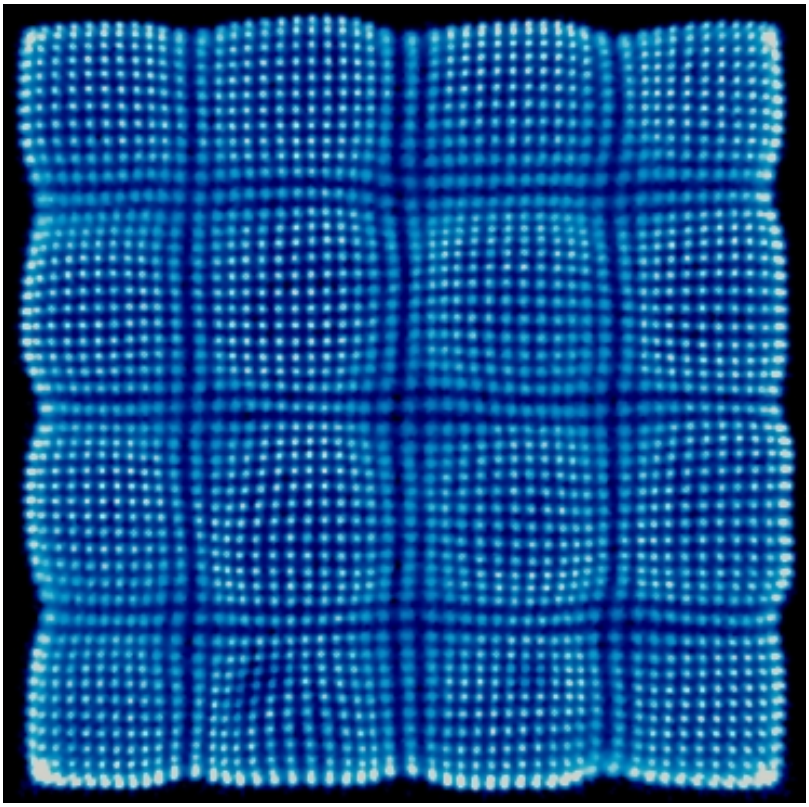

Figure 2R Reconstructed image obtains applying centroid algorithm on previous images.

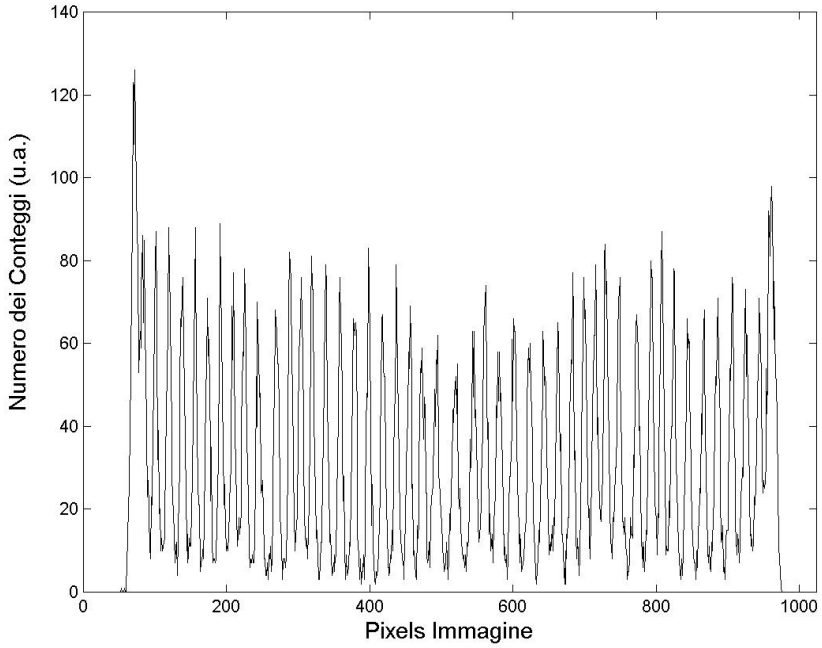

Figure 3R Image profile obtained by flood field irradiation of the camera

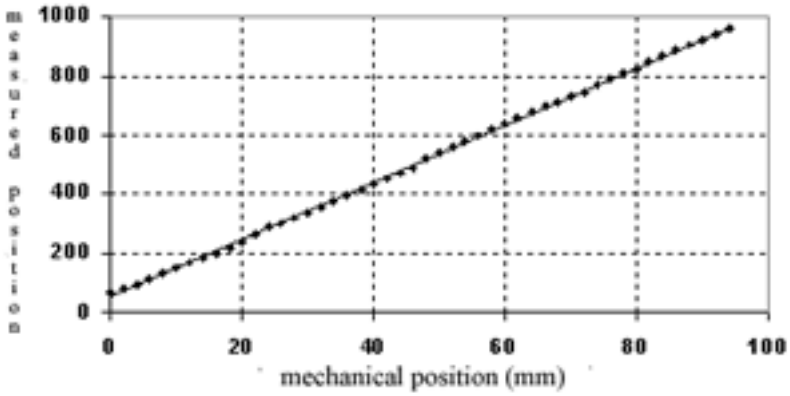

Figure 4R: Position linearity response for 16 PSPMT detector obtained by a 2mm step scanning of the detection area

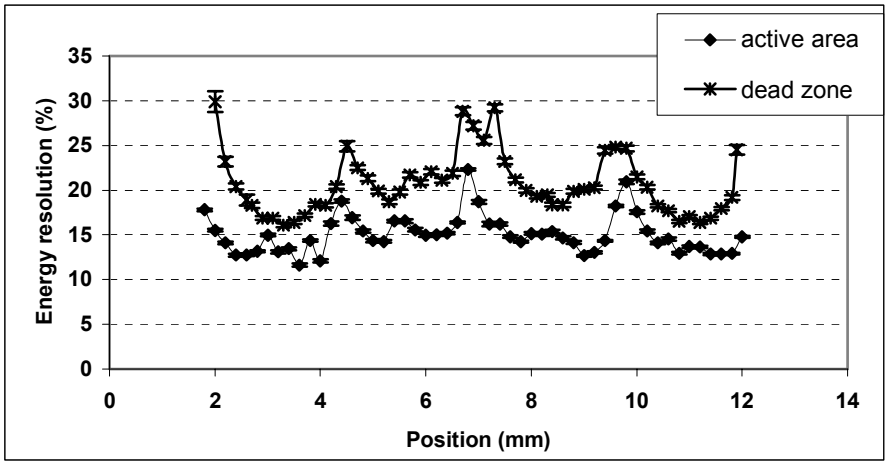

Figure 5R: Energy resolution response in active area and dead zones

Table 1R
Energy resolution

Active area (%)	**Dead zone** (%)
15,1±2,1	20.7±3,4

Spatial resolution

The spatial resolution of a gamma camera depends on an intrinsic factor (Ri) and a geometric factor (Rc) due to the collimator by:

$$R = \sqrt{R_i^2 + R_c^2}$$

The 16 PSPMTs gamma camera has a hexagonal parallel hole collimator with spatial resolution equal to 10 cm@ 9,67 mm FWHM SDC. The intrinsic spatial resolution for 16 PSPMTs gamma camera was obtained overlapping single pixel image obtained by previous scanning measurement, along a crystal row. The profile image FHWM of a single spot represents the intrinsic spatial resolution, calibrated on scanning step dimension.

Due to discrete structure of the detector, the intrinsic spatial resolution value is strongly function on detection area position. In figure 6R the spatial resolution profile in active area and dead zone are shown respectively and the mean values are reported in table 2R.

The overall spatial resolution value for 16 PSPMTs gamma camera was calculated studying the scintillation events distribution obtained by changing the source-collimator distance.

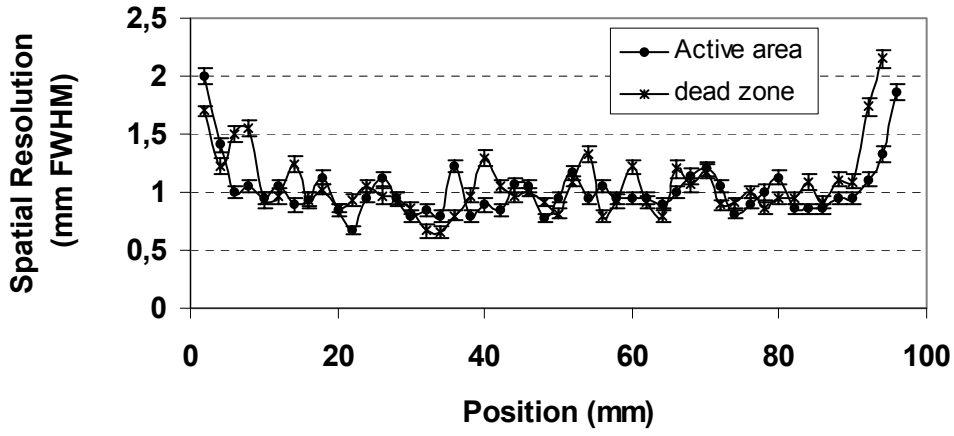

Figure 6R Intrinsic spatial resolutions of the range camera a16 PSPMTs

Table 2R
Intrinsic spatial resolution

Active area (mm FWHM)	**Dead zone** (mm FWHM)
1,02±0,24	1,06±0,28

A 3 mm ^{57}Co point source was utilized and 15cm, 10cm, 5cm and 0cm distances were set. The result is shown figure 7R, compared to Anger Camera one: the multiple camera introduces a spatial resolution better then Anger Camera for source-collimator distance less then 8cm

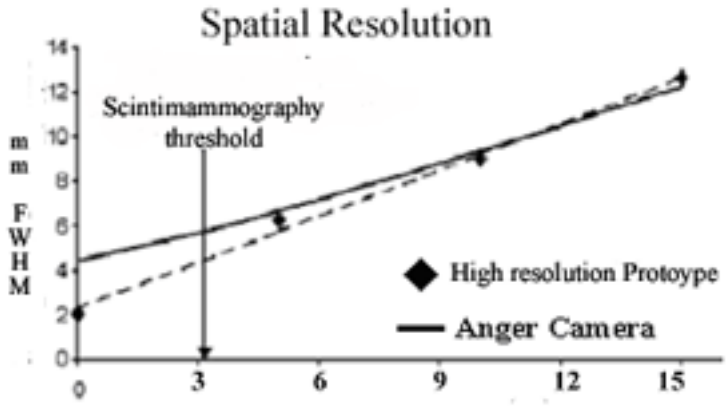

Figure 7R Spatial resolution of the 16 PSPMT camera and Anger Camera in function of source-collimator distance.

Prototype of large FOV high resolution gamma camera

For large FOV high resolution gamma camera the same calibration procedures of the 16 PSPMT was utilized. In figure 8R the reconstructed image by flood field irradiation is shown, with relative energy spectra and image profile, after gain calibration of each photomultiplier.

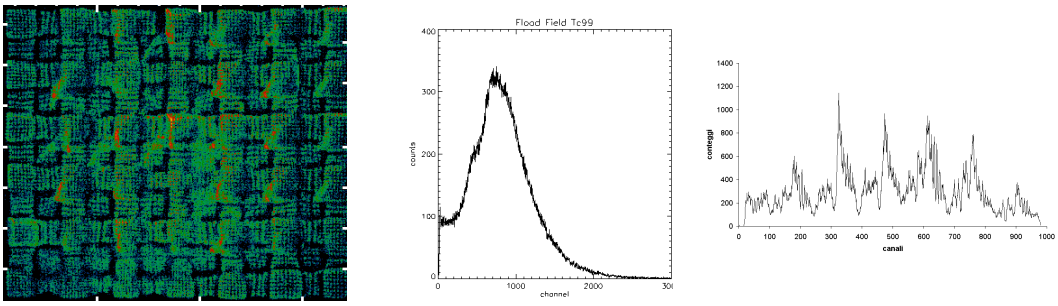

Figure 8R: Flood field irradiation by ^{99m}Tc source of the 42 PSPMT camera: raw image, energy spectra and relative profile of the image

Even if the scintillation events occurred in dead zones are well identified, the image is enough noisy, probably due to a no-optimization of reconstruction image method.

After LUT procedure, the corrected image however presents a counting homogeneity of 5% (see figure 9R). By flood field irradiation, the position linearity response has been obtained, shown in figure 10R. The spatial resolution values are reassumed in table 3R, with the energy resolution ones.

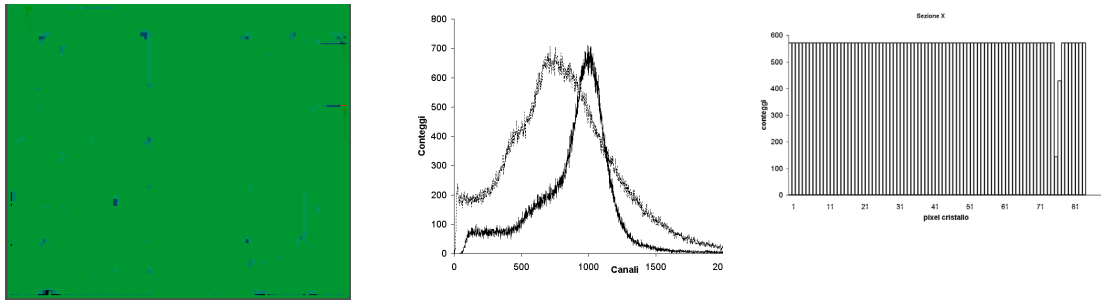

Figure 9R. Flood field irradiation of 42 PSPMTs camera: Corrected Image, energy spectra and relative image profile after LUT procedure

Table 3R

Energy and spatial resolution- 42 PSPMTs camera

	Active Zone	Dead zone	Peripheral zone
Energy resolution	(15±1)%	(26±2)%	(30±2) %
Intrinsic spatial resolution	0,8 mm	1,4 mm	-

Very high spatial resolution gamma camera prototype, integral assembly

Calibration measurements were performed by standard radioactive calibration sources and by capillaries filled with ^{99m}Tc and ^{125}I liquid sources. ^{125}I has a 59.4 days half-life and 27-35 keV gamma-ray emission while ^{99m}Tc has 6 hours half life and 140 keV gamma-ray emission. We utilized capillaries with an inner diameter (ID) ranging from 0.25 to 0.5 mm.

Due to the different emission energies, the measurements were performed with two beryllium-copper parallel-hole collimators (one high resolution and one high efficiency) dedicated for the ^{125}I and with a tungsten (19.3 gm/cc density) high efficiency parallel hole collimator and a tungsten-like (10.59 gm/cc density) high resolution parallel hole collimator. In addition, the imaging performance was also evaluated by two tungsten/copper pinhole collimators using 0.5 mm and 0.28 mm holes (90° angle and 1.125 mm hole to surface distance) and a general purpose collimator (see Table 4R for collimators characteristics).

To evaluate the position non-linearity and response in-homogeneity of detector, we performed a flood field irradiation utilizing a tungsten collimator (see table 4R) directly coupled to detector and a Co^{57} flood calibration source. The collimator was shifted in four different directions, by a fixed step, in order to cover the total detector surface. To obtain an exact calibration of detector surface we also scanned the surface in 1.5 mm steps with a Co^{57} 1mm point source. These measurements were compared with similar results obtained by 16 PSPMT gamma camera developed in IMI project.

Table 4R
Parallel hole collimators characteristics

Collimator	Hole ∅ (mm)	Length (mm)	Septa (mm)
Be/Cu High efficiency	0.364	10.6	0.105
Be/Cu High resolution	0.460	14.3	0.177
Tungsten High efficiency	0.364	10.6	0.105
Tungsten like High resolution	0.460	14.3	0.177
Tungsten Flood field (circular hole)	1.540	100.0	3.3 (center to center hole distance)
Pb General Purpose	1.500	22.0	0.200

The detector demonstrated very good scintillation light collection as is shown in Figure 10R , for ^{99m}Tc ^{125}I source. At 140 keV and 25-27 keV, the resulting energy resolution is 10% and 20% respectively. These are very good values if we take into account the typical low photocathode quantum efficiency (20-22% at 450 nm) and low gain uniformity of PSPMT.

In comparison with pixellated gamma camera 1, at 140 keV gamma ray energy, the planar assembly shows a superior energy resolution, 10% with respect to 20% (see Figure 11R) due principally to the planar structure of the crystal.

Charge distributions collected on the anode plane for a single interaction event are shown in Figure 12R for planar detector and pixellated camera respectively. The charge distribution of planar crystal resulted 12 mm FWHM, which is much wider than expected (7mm FWHM), probably due to light reflections from the back side. The value is 4 mm wider than scintillation array crystal.

From the precise calibration of detector surface we obtained the position response, shown in Figure 13R. The light distribution shape is larger than for pixellated camera,

and therefore the detector presents position linearity confined inside a central area of 30 mm size.

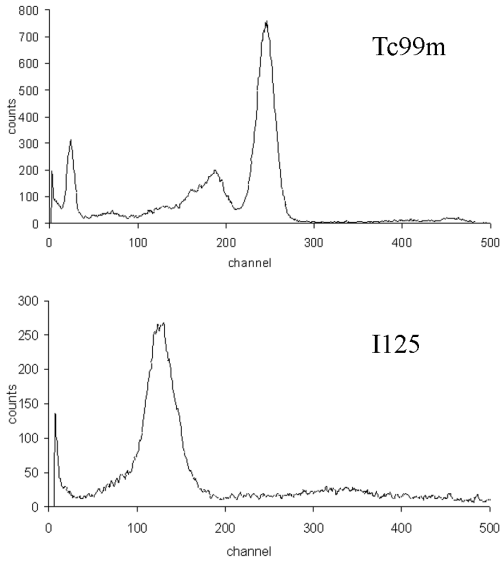

Figure 10R. Pulse height distribution for ^{99m}Tc (upper) and ^{125}I (lower) radioactive source.

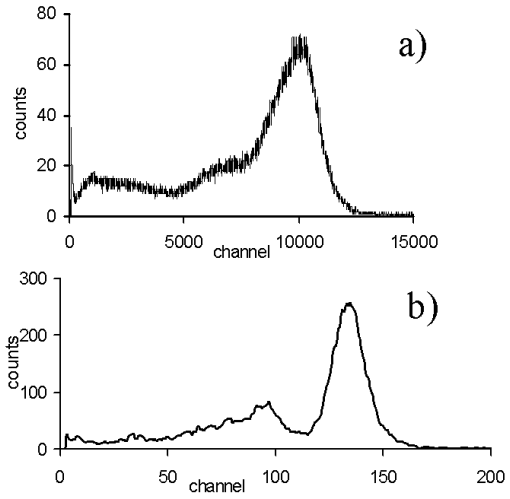

Figure 11R. NaI(Tl) pulse height distribution for a). pixellated camera and b). planar detector.

The MTF curves for both detectors were calculated using a 0.5 mm ID capillary filled with ^{99m}Tc. This line source was used to obtain LSF detector. The general purpose collimator was used for both cameras and compared with the intrinsic response of collimator simulated by a Monte Carlo. As is visible in Figure 14R, the MTF curve of NaI(Tl) planar crystal shows superior image performance.

The flood field image for planar detector is shown in Figure 15R with the relative profile. The image was acquired with a special tungsten collimator and a Co57 flood calibration source. The detector exhibits good linearity response, especially in central zone. This result can be improved by applying a GAUSS2D fit algorithm on the anode charge distribution to calculate the position on each event. In Figure 16R it is shown the lower left corner of flood field image obtained by calculating events position by a centroid algorithm (upper image) and by the GAUSS2D fit (lower image) where the improvement of the linearity response is highlighted.

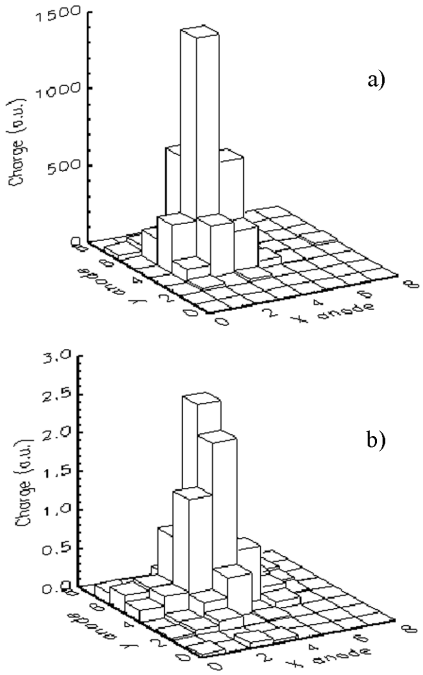

Figure 12R. NaI(Tl) charge distribution collected on the anode plate for a single interaction event for a) pixellated camera and b) planar crystal.

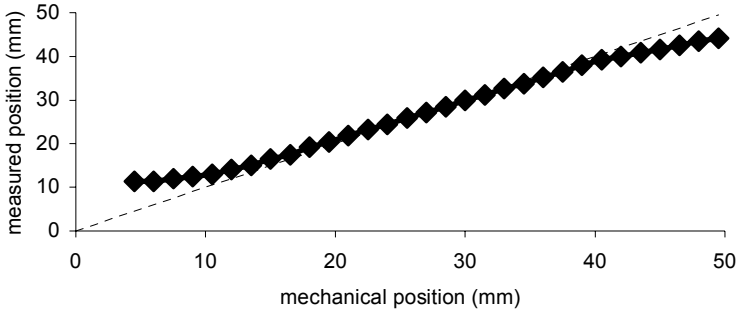

Figure 13R. Position response of planar crystal.

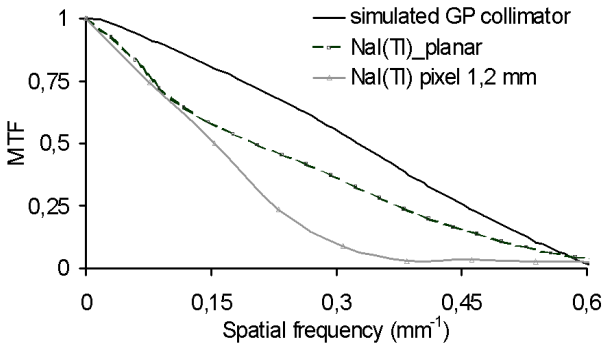

Figure 14R. MTF curves for planar crystal and pixellated camera in comparison with simulated collimator response.

To quantify the spatial resolution at 140 keV, in Figure 17R the images and relative profiles of two capillaries were compared, obtained by planar detector (Fig. 17a) and pixellated (Fig. 17Rb) respectively. The capillaries had an OD of 0.7 mm and an ID of 0.5 mm, were filled with ^{99m}Tc, and then placed at a 1.4 mm center to center distance. A

tungsten-like high resolution parallel-hole collimator was used. For planar detector the resulting spatial resolution was better than 0.7 mm while pixellated camera could not resolve the sources.

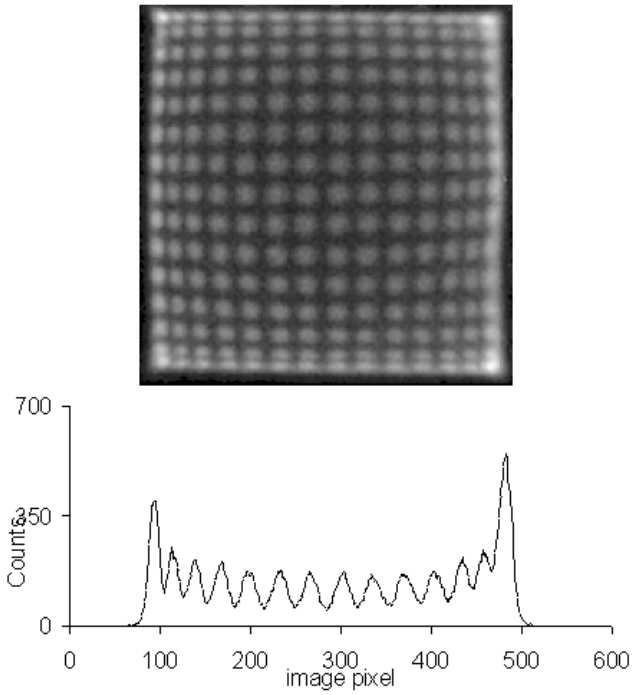

Figure 15R. Flood field image for planar detector and relative profile obtained with special tungsten collimator and ^{57}Co flood calibration source.

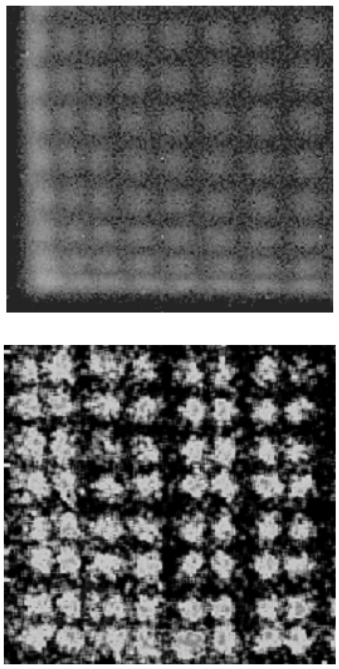

Figure 16R. Flood field image (lower left corner of Figure 15R) for planar detector obtained with flood field tungsten collimator and ^{57}Co flood calibration source with two different event position reconstruction algorithms: centroid algorithm (upper) and GAUSS2D fit of anode charge distribution (lower).

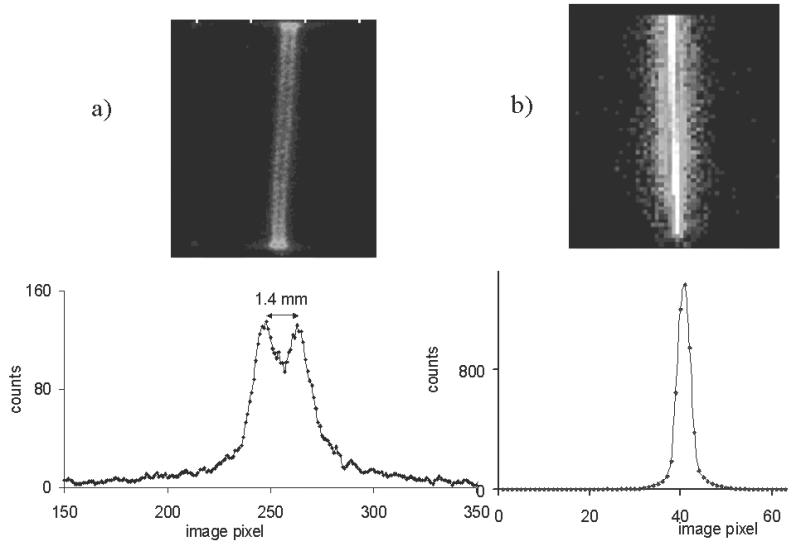

Figure 17R Images and relative profiles of two of 0.7 mm OD and 0.5 mm ID capillaries placed to 1.4 mm center to center distance, filled with ^{99m}Tc. Images were obtained with a). planar detector and b). pixellated camera, using tungsten-like high resolution parallel hole collimator.

The spatial resolution for the planar detector was determined by imaging two 0.7mm OD (0.5 mm ID) capillaries placed next to each other with a 0.4 mm OD cold tube between them (1.1 mm center-to-center distance); a tungsten high efficiency parallel hole collimator was used. The results are shown in Figure 18R, for imaging @140 keV; in this case we utilized the GAUSS2D fit to obtain the events position.

The intrinsic spatial resolution at ^{125}I emission energy was deduced by using a beryllium-copper parallel-hole collimator. Figure 19R shows the image profile obtained by a 0.3 mm diameter capillary filled with ^{125}I. No difference was observed in the spatial resolution value obtained when a high resolution and a high efficiency collimator were compared. The results show an intrinsic spatial resolution better than 2 mm (1.8 mm).

Images were also obtained with pinhole collimators in two extreme situations, one with a low magnification factor (low resolution) and good detection sensitivity and one with a high magnification factor and low detection sensitivity. In these two configurations we imaged two 0.3 mm ID (0.4mm OD) capillaries filled with 39 μCi of ^{125}I placed next to each other with a cold capillary (0.4mm OD) between them. Figure 20R shows the relative image profiles. For a 0.28 mm pinhole with a magnification factor of 10, we obtain a spatial resolution of 0.34 mm, for geometrical resolution of 0.3 mm and a radioactive line of 0.3 mm. In table 5R the spatial and energy resolution results are reassumed

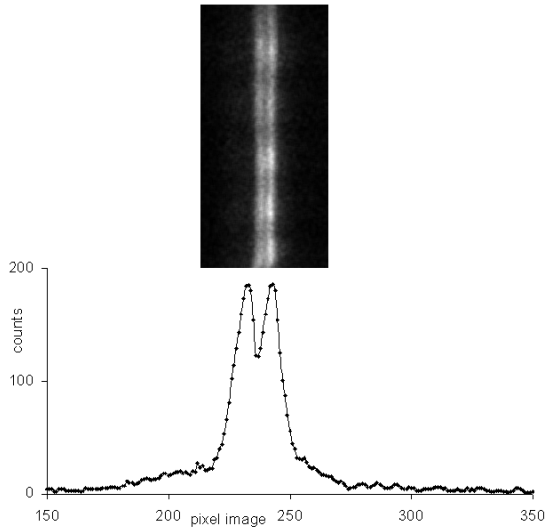

Figure 18R. Image and relative profile of two 0.5 mm ID capillaries filled with ^{99m}Tc, placed next to each other with a 0.4 mm OD cold tube between them (1.1 mm center-to-center distance) in the front of the high-efficiency tungsten collimator

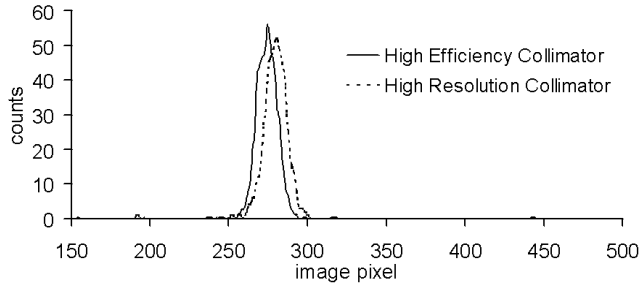

Figure 19R. Profile of a 0.3 mm capillary image obtained with Cu/Be parallel-hole collimator.

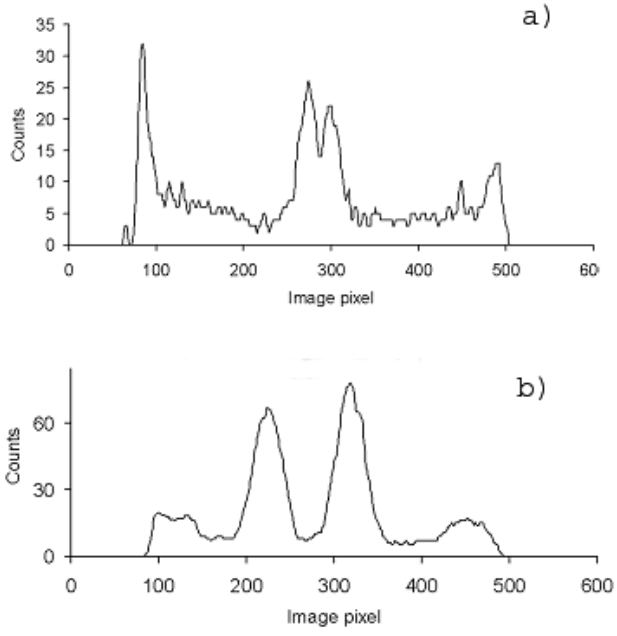

Figure 20R. Image profiles of two 0.3 mm ID (0.4mm OD) capillaries filled with 39 μCi of ^{125}I placed next to each other with a cold capillary (0.4mm OD) between them. Images were obtained with a) a 0.5 mm pinhole collimator and a magnification of 2.25 and with b) a 0.28 mm pinhole collimator and a magnification of 10.

Table 5R

	Tc^{99m} (140keV)	I^{125} (27 keV)
Energy resolution	10%	20%
Spatial Resolution	0.7mm	1.8 mm

Scintimammography: clinical trial

Like planned in IMI project, a scintimammography trial clinical using Anger Camera and high resolution gamma camera prototype was performed, in order to compare the results of both detectors. Twenty scintimammography images were collected and each patient was previously subjected to mammography analysis so as to obtain a dual modality image (RX and Gamma) of suspected lesions. After i.v. administration of 99mTc sestamibi (740MBq ≈ 10 ng) to patient, the two gamma images, with Anger Camera and with high resolution prototype was recorded. It is necessary to remember that the two images are acquired in two different projections: the Anger image is acquired in prone position, while the image by high resolution prototype is acquired in cranio-caudal projection, like in RX mammography.

In this chapter, the most important cases analyzed during the clinical trial are described in order to highlight the advantages offered by the new high resolution prototype respect to traditional Anger Camera in Scintimammography.

Case 1

In figure 21R RX and Anger Camera images of the sx breast are shown, where a tumoral lesion is well evident (see yellow circle in the mammography and the arrow in the scintimammography images). In Anger Camera image is present a large emission in the chest zone due to scattering coming from the patient body. In figure 22R the high resolution scintimammography images of both breasts are shown. The images confirm the presence of a tumoral lesion identifiable in high uptake zone. Also the image shows a strong reduction of the scattering component in the chest zone respect to Anger Camera, due to the very good performances of the prototype in term of spatial resolution. The high spatial resolution allows an optimal identification of the single pixel crystal contribution to the image and therefore to operate an effective gain correction of the energy with consequent elevated reduction of the scattering component by the body.

By the pixel-crystal number involved in image lesion, the deduced dimension of the tumor is 2 cm diameter. The image profiles of the sx breast in correspondence of the tumoral lesion are shown in figure 23R, in perpendicular (A) and parallel (B) direction respect to the chest. From the total image and the profiles it has been possible to calculate a medium value of SNR equal to 35.

In figure 24R finally the dual modality Rx and Gamma image is shown, obtained applying a particular algorithm of fusion of RX and Gamma image by the high resolution prototype. The position of the suspicion lesion in the RX image fits with the zone with maximum uptake in gamma image, confirming the diagnosis of a breast cancer. Like previously described, the visibility of the lesions in the clinical images typically is estimated in terms of SNR. By the Anger image the obtained mean value of SNR was 7.35 respect to 36 by the prototype, for a percentage increment of approximately 80%.

The lesion was subsequently removed confirming the dimensions deduced by gamma images (2 cm diameter).

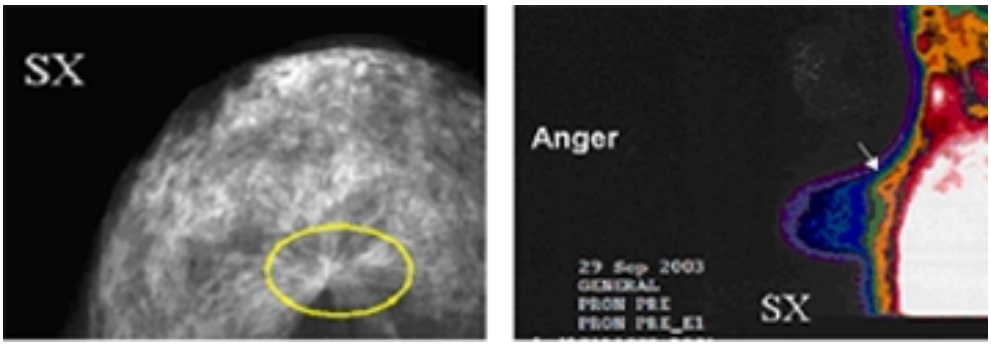

Figure 21R: RX and Anger Camera Images of sx breast (case 1). The yellow circle indicates suspect structure with 1.5- 2 cm dimension. In the scintimammography image the white arrow indicates a zone with high uptake typical of a tumoral lesion presence.

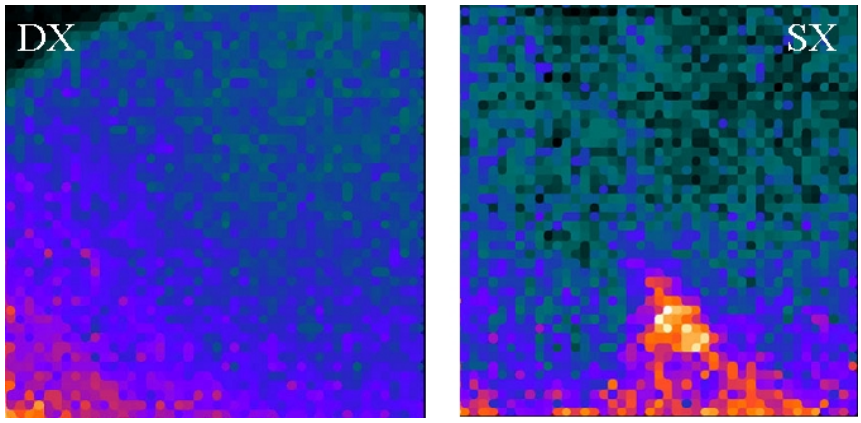

Figure 22R: High resolution scintimammographic image by gamma camera prototype. In the sx breast image is evident a zone with high uptake typical of the presence of a tumoral lesion.

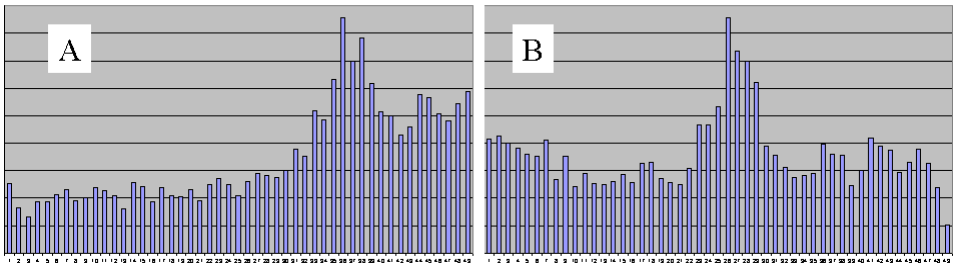

Figure 23R: Profiles of sx breast image shown in fig.22R in correspondence of the breast cancer. A) profile in perpendicular direction to the thorax, B) profile in direction parallel to the thorax

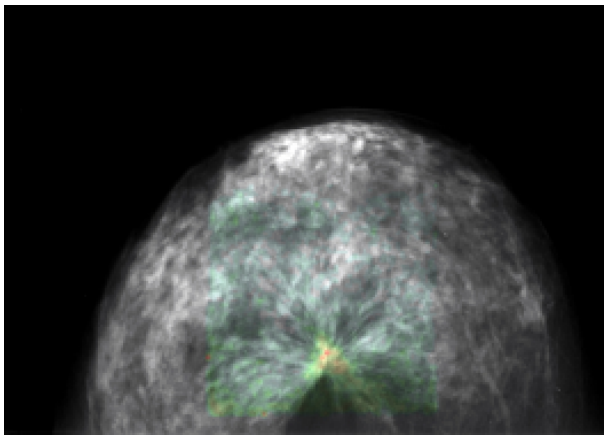

Figure 24R: Dual Modality image obtained by Rx and high resolution Gamma image

Case 2

The patient had a suspicious ductal tumoral lesion in the sx breast. For its peculiarity, this kind of lesion is not easy to early diagnose because it takes the shape of lactiferous duct within is developed and it reaches detectable dimensions only when the tumor is already evolved in metastasis.

In figure 25R RX sx breast images in three different projections are shown. The circles evidence the zones containing the lesion; in particular, the B image was obtained by operating a partial compression of the breast in order to see better the lesion.

The lesion dimension, approximately 7 mm, represents an inferior limit of the detection with Anger Camera. The figure 26R shows scintimammography image obtained by Anger Camera; the white arrow indicates the hypothetical position of the tumor, but the low spatial resolution and contrast of the image don't allow an identification of the lesion. In any case the RX and scintimammography images obtained by Anger Camera have provide useful information about the identification of the lesion in the high resolution gamma image by prototype. In fact in figure 27R the high resolution gamma image is shown with the relative zoom on the suspected zone

involved in the lesion. The obtained SNR mean value was 13; the surgery confirmed a breast cancer of 7.7 mm

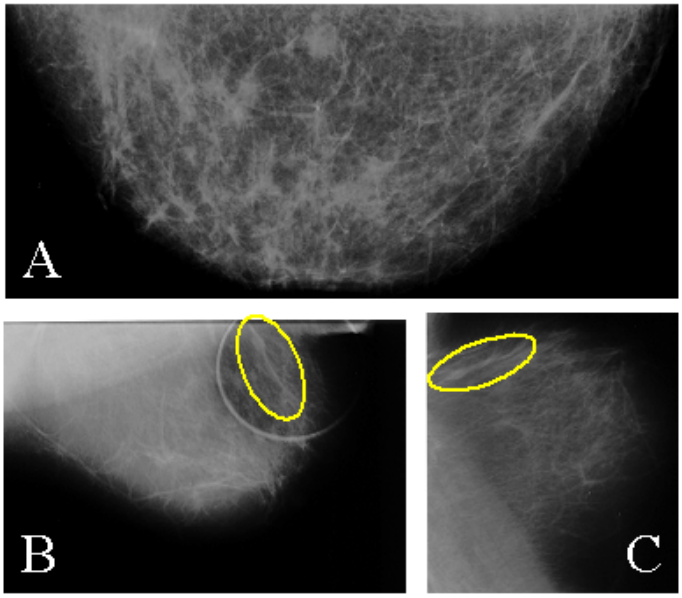

Figure 25R. RX sx breast images in three different projections. The circles evidence the zones containing the lesion. The B image has been obtained operating a partial compression of the breast.

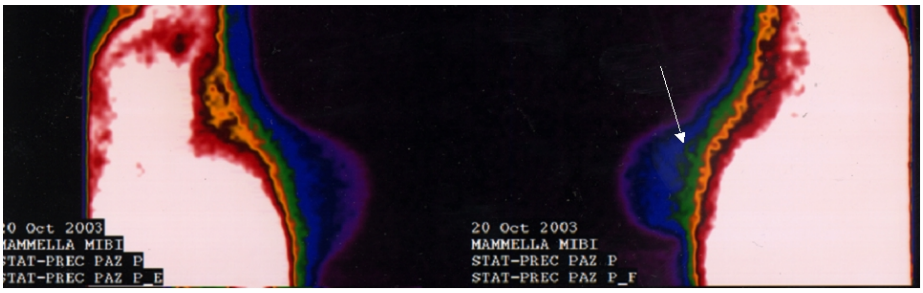

Figure 26R. Anger Camera Scintimammography for Case 2. The white arrow indicates the hypothetical position of the tumor

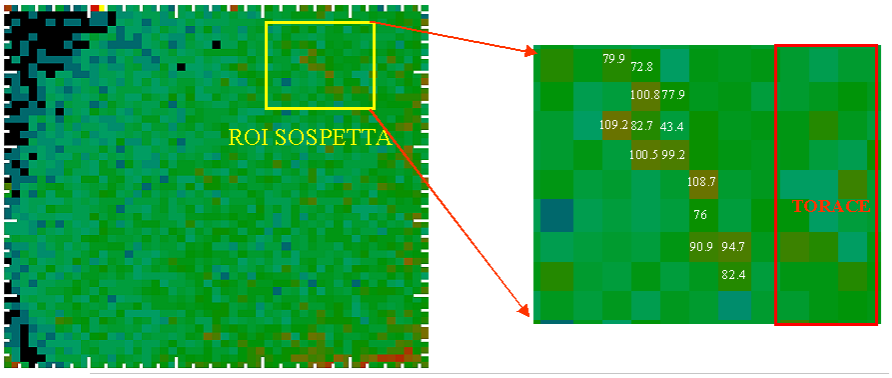

Figure 27R: High resolution gamma image by gamma camera prototype, Case 2. On the right a zoom of the image highlights the presence of the lesion.

Case 3

In this paragraph a particular case is discussed, regarding a young patient (29 y.o.) with breast cancer suspicion detected by echography analysis of right breast (see figure 28R). Prone lateral scintigraphy was obtained 15 min after 99m TC injection by a double headed Anger camera equipped with a general purpose parallel hole collimator (see figure 29R). High resolution scintigraphy was performed in cranio-caudal projection 30 min after the radiotracer administration. By comparing conventional and high resolution images, Anger camera images showed a defined hot spot in the inferior field of right breast, highly suggestive of malignant lesion (see yellow circle in figure 29R). On the contrary, the high resolution scan shows an area with a large and inhomogeneous tracer uptake (see figure 30R). This evidence permits to suppose that probably the lesion in no malignant, because of a no-localized uptake area. The bioptical analysis confirmed the diagnosis about an inflammatory lesion.

Although the small breast length (6 cm), the posterior breast portion (close to the chest) was well imaged thanks to the narrow overall dead zone of the camera (13 mm) and to the good suppression of radiation scattered by chest.

This result shows how high resolution approach to breast scintigraphic scan, is not only able, as previously demonstrated, to improve the diagnosis sensitivity in non palpable lesions, but also it shows that the obtained image allows to better categorize the lesions in function of morphology of the tracer spatial distribution in breast tissue

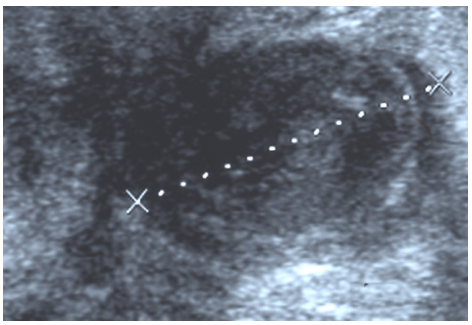

Figure 28R: Echography image of suspicious lesion (Case 3)

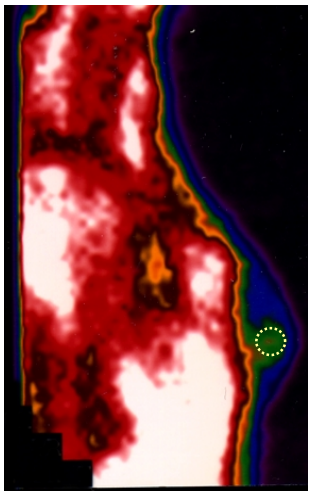

Figure 29R: Anger camera image (Case 3). The yellow circle indicates the area containing the suspicious lesion.

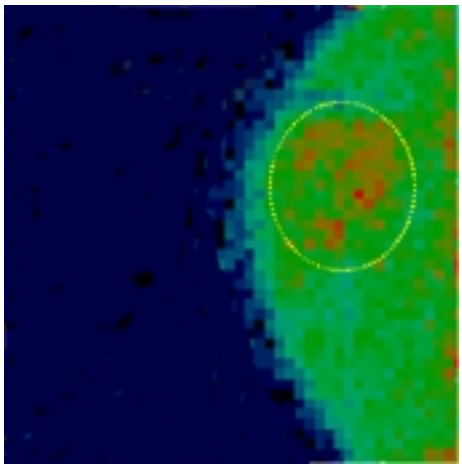

Figure 30R: High resolution camera breast image (Case 3). The higher uptake is reported in red. The yellow circle indicates the lesion

Analysis of high resolution scintimammographic images by MIA algorithm

To test the MIA algorithm, two sets of windows were prepared. The first set named Windows#1 is shown in Fig. 12MA on top of imager spectrum. Channels range corresponding to the Windows#1 and Windows#2 set are shown in Table 6R. These energy windows represent a new set of 'variables' (see Appendix) chosen to approximate the spectrum detected by each detector in the imager. Variables set named Windows#1 (see Fig.12Ma and Table 6R) has three windows (w_1, w_2 and w_3) delimiting the energy range corresponding to Compton scattering, and two windows w_4 and w_5 that select the photopeak. In the set of variables named Windows#2 (see Table 6R) only the first one variable w_1 collects the Compton scattered radiation, whereas windows w_2-w_5 map the photopeak energy region. In both set window w_6 collects photons in the high-energy tail of spectra. As evident, variables w_1-w_6 approximates the spectra detected by all detectors in the imager. The Mean photons count in Table 6R indicates that variables Windows#1 roughly reproduce the profile of the photons energy distribution shown in Fig.12Ma., on the contrary variables Windows#2 gives emphasis to the energy region delimiting the photopeak. Standard deviation in the last column indicates the range variability of each variable.

Multivariate imaging is data reduction technique that groups the information contained in variables w_k in a limited number of factors known as score images. The analysis of a scintimammography showing a tumor is made evident by loadings vectors and score images shown in Table 7R and in Fig. 31R, respectively. The multivariate

image analysis algorithm shown in Fig.32Rb is equivalent to the matrix decomposition of a two-dimension matrix **X**, like as $\mathbf{X} = \mathbf{t}_1\mathbf{p}_1^T + \mathbf{t}_2\mathbf{p}_2^T + ... + \mathbf{t}_6\mathbf{p}_6^T$ (1).

Table 6R
Windows approximating the imager spectra

Windows #1			
Windows	Channels	Mean	St. Dev.
w1	100 – 250	63.34	60.71
w2	251 – 380	110.76	79.52
w3	381 – 500	63.25	44.44
w4	501 – 600	39.51	24.95
w5	601 – 800	21.48	15.70
w6	801 – 1000	0.76	1.05
Windows #2			
Windows	Channels	Mean	St. Dev.
w1	100 – 450	216.50	162.72
w2	451 – 500	20.84	14.84
w3	501 – 550	17.03	11.91
w4	551 – 600	22.47	14.62
w5	601 – 750	21.12	15.50
w6	751 – 1000	1.12	1.52

After the reorganization, columns of matrix **X** contains the original variables w_k, and the matrix rows the spectra measured by all detector in the imager, resulting from the Windows approximation. Equation **(1)** indicates as **p** and **t** the loadings and the scores vectors, respectively, and as $\mathbf{tp}^T$ the outer product between vectors **p** and **t**. The scores image $\mathbf{T}_k$ shown in Fig.31Rb is obtained by reorganizing the corresponding scores vector $\mathbf{t}_k$ as an image. In vector to image reorganization the elements in vector $\mathbf{t}_k$ are converted in pixel image.

As detailed elsewhere, loadings vectors shown in Table 7R can be read as the correlation between the original variables, w_k, and the scores $\mathbf{t}_k$. This can be made evident by considering that each term in Eq. (1) is a fraction of total number of photons collected in each window w_k. The first scores images, $\mathbf{T}_1$, shown in Fig. 31R, collect the larger amount of photons reaching the detector (about the 89% an 99% of the radiation resumed in the Windows#1 and Windows#2 data set, respectively). This radiation is distributed to each variables w_k following the coefficient of vector loadings $\mathbf{p}_1$. It is worth to note that loadings $\mathbf{p}_1$ in Table 7R and Mean in table 6R have the same behavior as function of w_k. Following this approach we can consider scores $\mathbf{T}_2$ in Fig.31Ra collecting photons originally belonging to all energy windows (see loadings $\mathbf{p}_2$), and scores $\mathbf{T}_6$ in Fig.31Ra and Fig.31Rb to describe the local differences in the number of detected photons due to the presence of the dead zones among the PSPMTs. Finally, by comparing the remaining scores images $\mathbf{T}_3$-$\mathbf{T}_5$ in Fig.31Ra, and $\mathbf{T}_2$-$\mathbf{T}_5$ in Fig.31Rb, with the corresponding loadings vectors it appear evident that these images gives reason of

photons coming from limited regions in breast having a higher concentration of radiotracer; i.e., the tumor region and the nipple. In other word the increased number of photons emitted by this region changes the profile of spectra detected in a limited area of the imager inducing a local correlation. Multivariate imaging identifies these spectra, and shows the corresponding breast region in separated images.

Image reconstruction

As made evident in other field of applied spectroscopy, multivariate analysis of a series of spectra brings to light relevant features of the phenomenon under study; features originally masked by complex structure of spectra. The same is true for multivariate analysis of scintimammographic data. Since a relevant fraction of the radiation collected by all detectors in the imager is reduced in the first and second principal factor, the remaining scores can be used to produce a scintimammographic image where regions showing a high Tc^{99m} uptake are the most important ones (see Appendix for the image reconstruction procedure).

TABLE 7R
LOADINGS VECTORS

Windowing#1						
	p1	p2	p3	p4	p5	p6
w1	0.51	0.84	0.14	0.06	-0.03	0.00
w2	0.73	-0.34	-0.50	-0.30	0.08	0.00
w3	0.39	-0.36	0.32	0.70	-0.36	0.00
w4	0.19	-0.20	0.75	-0.60	-0.08	0.00
w5	0.12	-0.10	0.24	0.25	0.93	0.00
w6	0.00	0.00	0.00	0.00	0.00	1.00
Windowing#2						
	p1	p2	p3	p4	p5	p6
w1	0.99	-0.13	-0.03	-0.03	0.01	0.00
w2	0.08	0.36	0.19	0.63	-0.66	-0.02
w3	0.06	0.41	-0.12	0.55	0.72	-0.04
w4	0.06	0.67	-0.59	-0.40	-0.18	0.02
w5	0.07	0.49	0.77	-0.38	0.14	-0.01
w6	0.00	0.01	0.02	0.04	0.02	1.00

Multivariate analysis of the data set Windows#1 (Fig.31Ra) and Windows#2 (Fig.31Rb) points out that the tumor is evident in more than one scores images. Figures 32Rb were computed by scores $\mathbf{T}_3$-$\mathbf{T}_4$ (Fig.32Rb1 and $\mathbf{T}_3$-$\mathbf{T}_5$ (Fig.32Rb2) of Windows#1. At visual inspection Fig.32Rb1 seems noisier than Fig.32Rb2; however, in both the images the tumor, the nipple and the anatomic structure indicated by the arrow (Fig.32Rb2) are better evident than in Fig.32Ra; i.e., the conventional photopeak scintimammography. Figures 32Rc were computed by adding an increasing number. The vector products between scores images $\mathbf{T}_2$, $\mathbf{T}_3$ and the corresponding loading vectors

gives the image shown in Fig.32Rc1; images, in Fig.32Rc2 and Fig.32Rc3 were computed adding the vector product containing the score images $\mathbf{T}_4$ and $\mathbf{T}_5$, respectively, to the previous images. At visual inspection, it is evident that Fig.32Rc1 shows the tumor with a better detail than Fig.32Rc2 and Fig.32Rc3; i.e., the multivariate analysis of Windows#2 data-set compresses information regarding this regions of interest principally in score $\mathbf{T}_2$ and $\mathbf{T}_3$, whereas the remaining scores collect information about the background emission. Is evident also that all images in Figures 32Rb give better evidence to the breast profile, the tumor and the nipples than the photopeak scintimammography (Fig.32Ra). As general consideration, by observing Figures 32Rb and 32Rc, it seems evident that the score images collecting the main fraction of the background radiation and the Compton scattering gives scintimammographic images easier to read than the conventional photopeak scintimammography.

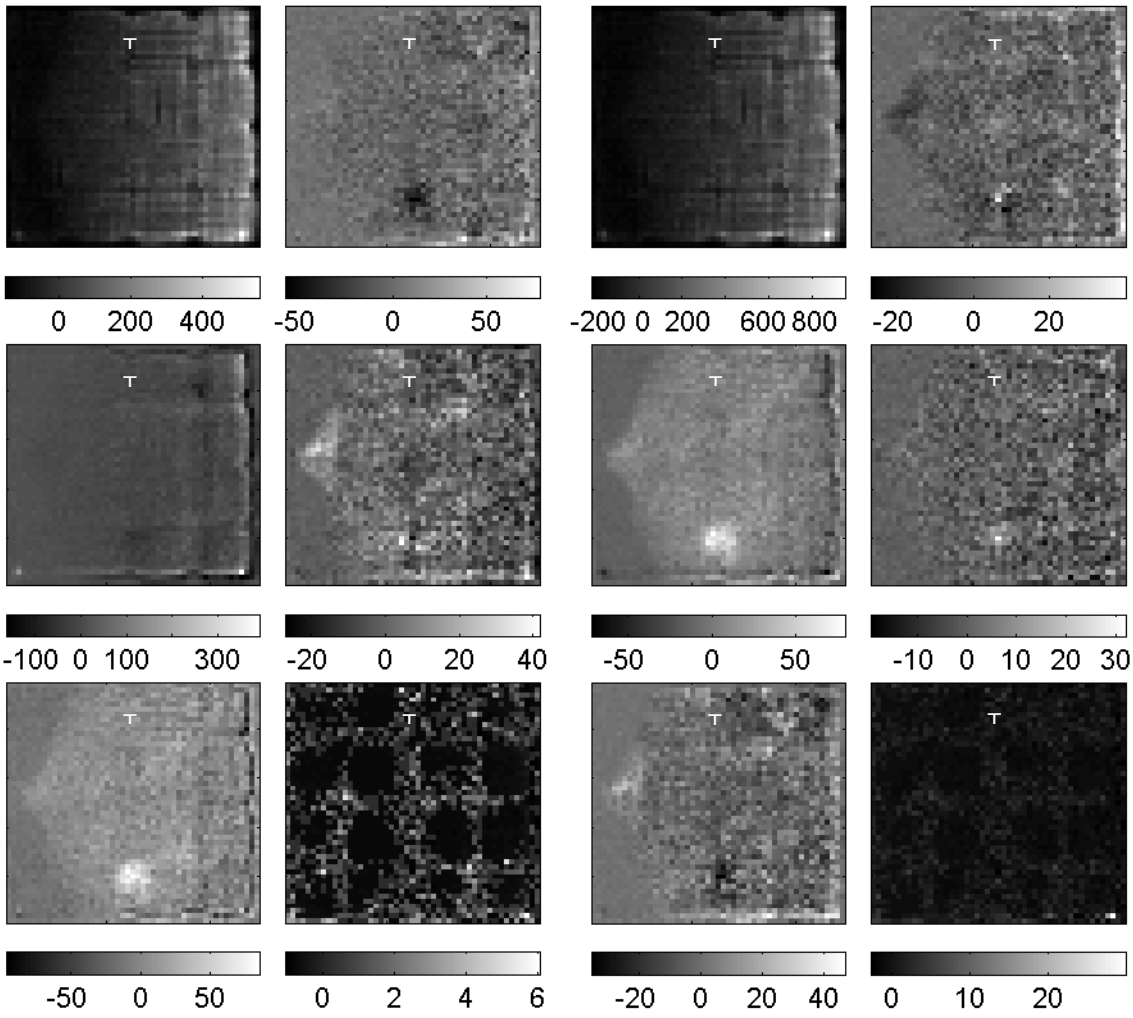

Figure 31R**. Scores images resulting from MIA on A) Windows #1 and B) Windows #2 set of images. Data in parenthesis indicates the percent of variability explained by the scores image.**

To put in evidence how the multivariate imaging technique woks, the analysis of two different clinical cases are shown in Fig.33Ra and Fig.33Rb, respectively. As indicated before, Fig.33Ra1 and Fig.33Rb1 display the photopeak images. The multivariate images are shown in the same column. Images reconstructed from MIA Images were computed by using all the scores images showing the tumor. Images in the left column reveal the presence of a big tumor with an irregular shape near the chest. By comparatively evaluating these images, it appears that the conventional technique (Fig.33Ra1) gives a high contrast image than one computed by MIA; namely the image resulting from the data-set Windows#1 (Fig.33Ra2). The same is not true by comparing Fig.33Ra1 and the image reconstructed from the data set Windows#2 presented in Fig.33Ra3, where the tumor profile is given with better evidence than in Fig.33Ra1. It is worth noting that a different contrast between the region containing the tumor and the background is evident also by comparing MIA images in Fig.32Rb2 and Fig.32Rc3. This result may be tentatively explained by considering that multivariate imaging employs all the spectrum profile and that the image depends on the set of windows approximating the imager spectra. In these terms, since the data set Windows#2 put the attention to the energy region delimiting the photopeak, the image resulting from MIA looks like to the conventional scintimammography, without the Compton scattering contamination. In Windows#1 data set the spectrum profile is reproduced with better accuracy this information, is preserved by the multivariate-imaging algorithm computing variables w_k by using scores images containing the tumor. By comparing images in Fig.32Rb2 and Fig.33Ra2 with images in Fig.32Ra3 and Fig.33Ra3 is evident that Windows#1 approximation reduces the image contrast but puts in better evidence local concentration of radiotracer like the nipple and the structures pointed by the arrow.

This interpretation seems confirmed by images in the right column of Fig.33Rb. Scintimammography shown in Fig.33Rb1 was performed on an uncompressed breast to confirm the presence of a local density variation previously diagnosed by the ultrasound scanning. The increased concentration of radiotracer evident in Fig.33Rb1 around the nipple (see arrow) confirms the presence of a suspected region to be better investigated. The Tc99 distribution appears better detailed in Fig.33Rb2 by the increased concentration in the region above the nipple. The same is not true in Fig.33Rb3; i.e., in the images resulting from the MIA of data set Windows#2, where the greater Tc99 uptake is shown as a uniform spot including the nipple.

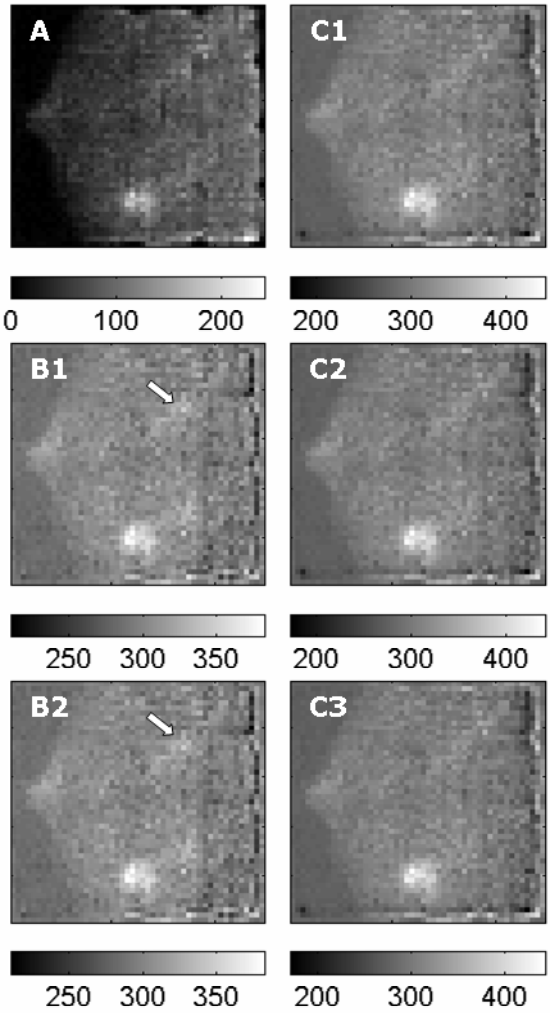

Figure 32R. **Conventional scintimammographic image is shown in Fig.32Ra. Figures 32Rb and 32Rc show images reconstructed by the MIA algorithm by using score images shown in Fig.31R.**

In conclusion the multivariate image analysis is a powerful data reduction technique that gives the possibility to differentiate the contribution due to scattering radiation from the directly emitted photons. Results show the realistic possibility to depict scintimammographic data as a series of images known as principal components where the Compton scattered radiation and the tumor region are shown as separated images This separation put in better results all the information detected by the scintimammographic imager, and improves the quality of the image resulting from multivariate analysis. As a consequence breast regions with a high Tc^{99m} activity also in the proximity of chest are shown with better evidence. The choice of the energy windows used to approximate the spectra detected by the imager, allows putting in evidence the tumor region as well as the local concentration of radiotracer by increasing the image contrast. This results looks promising and need to be better studied in terms of signal to noise ratio between the tumor and the background regions. To better define the

efficiency of multivariate imaging to analyze scintimammographic data, a series of experiment on a dedicated breast phantom are been undertaken to define the sensibility the technique in the presence of a different degree of Compton contamination.

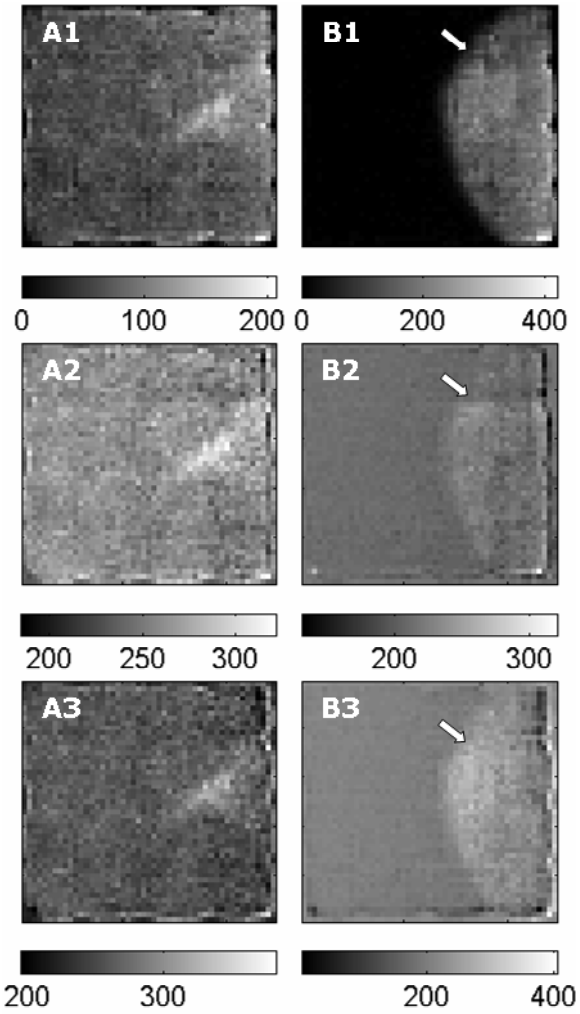

Figure 33R. Scintimammographic images describing two distinct clinical cases. The photopeak images and corresponding multivariate imaging results are shown in the left and right column respectively (see text).

Very high spatial resolution gamma camera prototype, integral assembly: *in vivo* experiment

The mice images were part of a study of inflammatory bowel disease (IBD), the second most common chronic inflammatory disorder in the world. A gut-specific vascular adhesion molecule expressed during intestinal inflammation (MAdCAM-1) was chosen as the target protein. MAdCAM-1 is an endothelial adhesion molecule that regulates lymphocyte transport in the gut and its expression is greatly up regulated in the inflammation presence, both in animal and in human tissue.

In this study, we used the MECA-367 antibody, a rat IgG against murine MAdCAM-1, and the SAMP1/YitFc murine model of IBD, a model that spontaneously develops intestinal inflammation with 100% penetrance by 30 weeks of age. Four 25 g SAMP1/YitFc mice were injected with 375, 125, 60 and 30 μCi of ^{125}I-labelled MECA-367. Images were collected immediately and two hours post-injection in order to evaluate the dynamic uptake of activity in the bowel. Two healthy Aldo-Keto Reductase (AKR) mice without bowel inflammation were used as controls, and were injected with the same antibody at a dosage of 150 and 60 μCi radioactivity, respectively. The *in vivo* measurements were performed with both beryllium-copper collimators.

To better evaluate the *in vivo* performances of the integral assembly detector, we acquired images of mice also with a dual modality (X-ray and gamma-ray) camera dedicated for small animal imaging. The X-ray images were obtained with a high resolution detector utilizing a 2k*2k Thomson CCD chip with a pixel size of 29 microns and a micro-focus x-ray source, while the gamma images were acquired by a gamma camera made by 2x2 H8500 Hamamatsu PSPMT array coupled to a NaI(Tl) scintillator array with 1.5 x 1.5 x 6 mm pitch (pixellated gamma camera 2 – PGC2). Gamma images were superimposed upon the digital radiograph to enhance the anatomical localization of the ^{125}I uptake. A barium-sulfate suspension was administered to all mice to improve the bowel structure identification in the X-Ray image.

Mouse images

In Figure 34R we show the gamma ray image, obtained by the PGC2 and the dual modality image of an AKR control mouse 2 hours post-injection of 60 μCi ^{125}I-labelled antibody. The presence of the barium contrast medium operates as an attenuator for X-ray transmission, with structures such as the stomach and cecum (white circle) being clearly visible in the digital radiograph. The cecum and colon are also visible in the ^{125}I image, appearing as a circular zone with low activity (white circle). The good spatial resolution of the x-ray camera permits visualization of the lack of Barium in the center of this region (see arrow).

Images of the AKR control mouse obtained with NaI(Tl) integral assembly detector and dual modality gamma camera are presented in Fig 35R. Comparison of the NaI(Tl) integral assembly detector image to the dual modality image shows a superior spatial resolution that allows a more detailed information around the cecum and large intestine. In addition, the image details portions of the higher intestinal tract (stomach, duodenum,

jejunum, and ileum) and can distinguish intestinal segments containing radioactivity from the high-uptake regions observed in the liver.

Figure 36R shows the PGC2 image and merged dual-modality images of a SAMP1/YitFc mouse with bowel inflammation taken 2 hours post-injection of 30 µCi ^{125}I-labelled MECA-367. The increased uptake of radioactivity in the intestinal zone is due to the presence of inflammatory disease and increased expression of the MAdCAM-1 target protein. High levels of activity obscure barium attenuation of ^{125}I X-rays, but the diseased region is clearly separated from the activity associated with the pulmonary circulation and liver uptake.

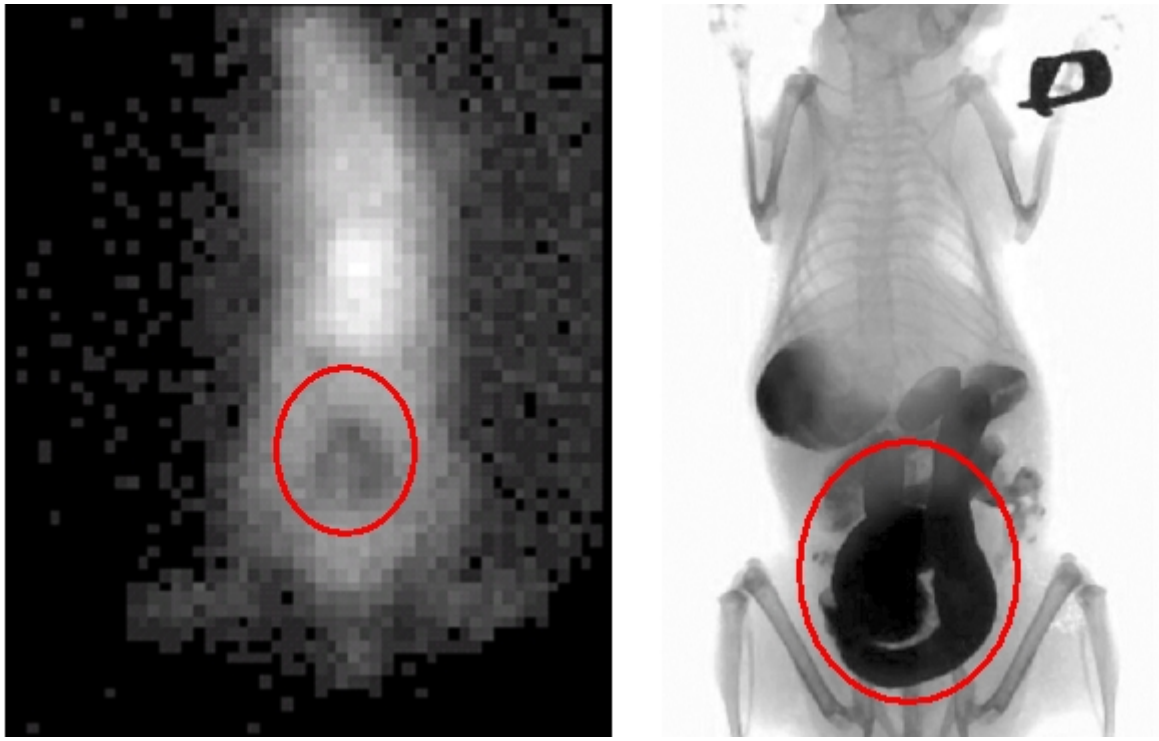

Figure 34R. Gamma ray image (left), obtained with the PGC2, and the dual modality image (right) of an AKR control mouse 2 hours post-injection of 60 µCi ^{125}I-labelled antibody with the Be/Cu high efficiency collimator. The white circle indicates the X-ray attenuation of the barium. The cecum and colon are also visible in the ^{125}I image, appearing as a circular zone with low activity (white circle). The improved spatial resolution of the camera permits visualization of the lack of Barium in the center of this region (arrow).

The same image obtained with the NaI(Tl) integral assembly detector is presented in figure 37R. In this image it becomes apparent that the inflammatory disease is localized to the terminal ileum (adjoining the cecum). It is also possible to distinguish the intestinal uptake from radioactive accumulation in the bladder. These results are consistent with histological evaluation of intestinal tissue samples, which have shown that SAMP1/YitFc developed inflammation that is most severe in the terminal ileum. All images of mice presented were obtained by the high efficiency Be:Cu parallel collimator.

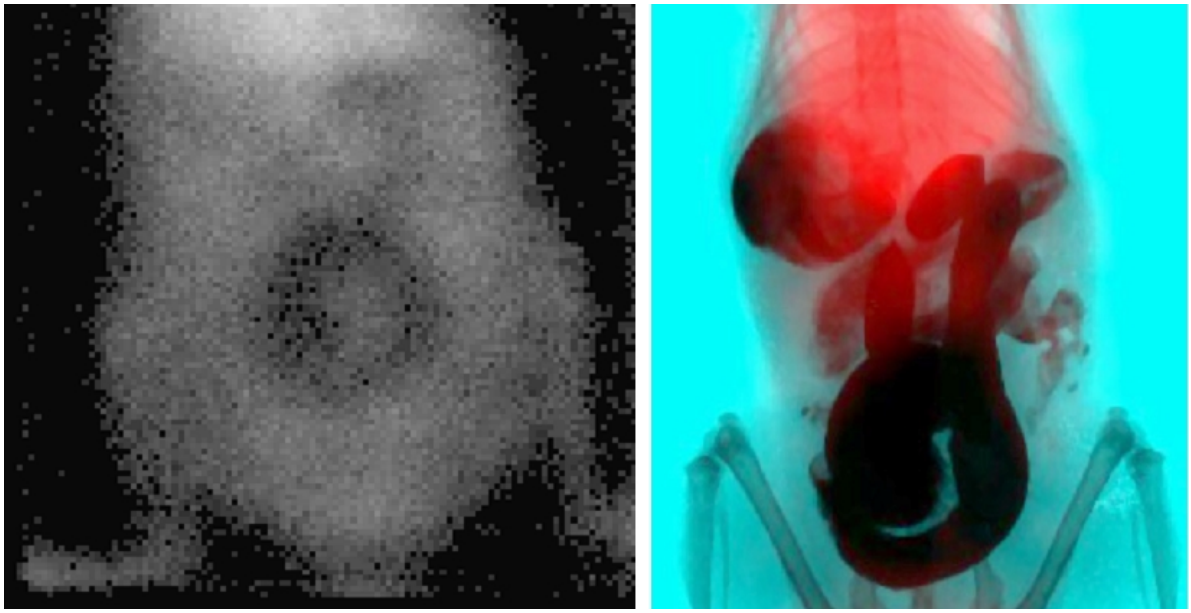

Figure 35R: Gamma-ray image with the NaI(Tl) integral assembly detector (left) and a dual modality image (right) of the 60 µCi control mouse 2 h after the injection (Be/Cu high efficiency collimator).

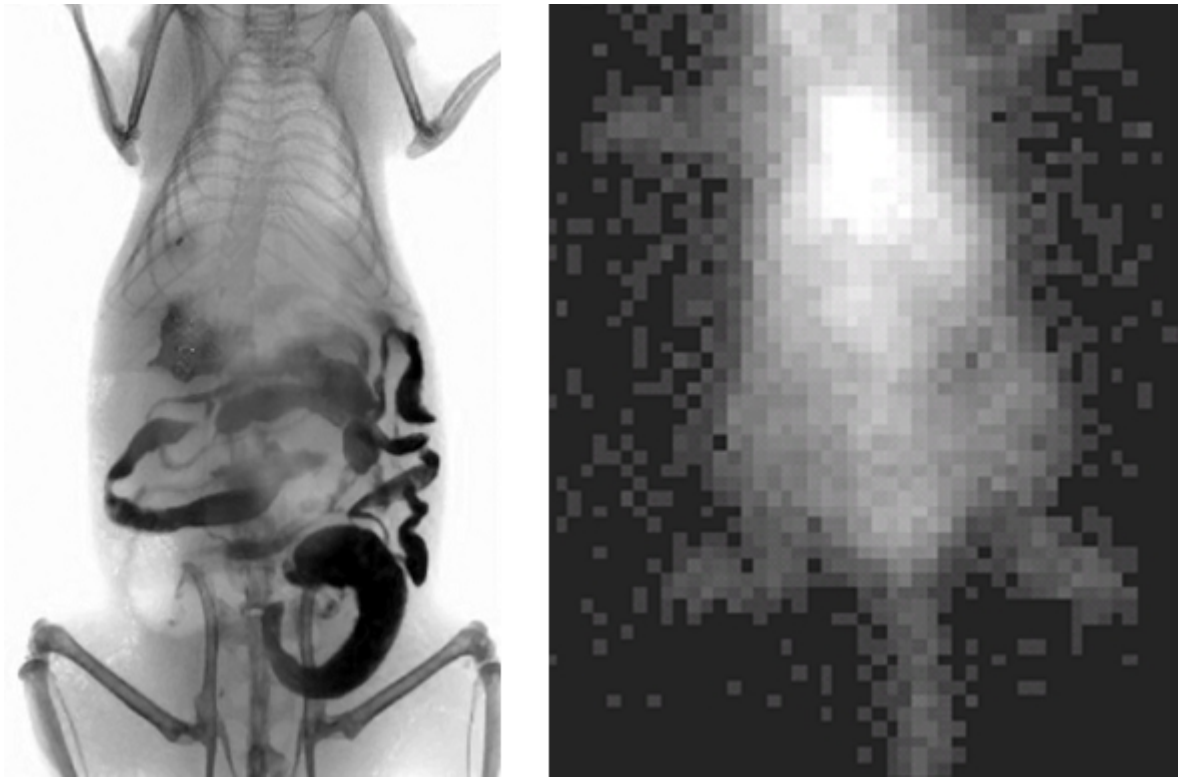

Figure 36R. Gamma-ray image from 2x2 flat panel camera and dual modality image of the 30 µCi mouse 2 h after the injection. (Be/Cu high efficiency collimator).

In terms of in vivo imaging performance of this detector, the results are very impressive. The images of SAMP1/YitFc injected with 30 µCi activity show inflammation throughout the intestinal tract, with the disease very well defined at two hours post-injection. The NaI(Tl) integral assembly detector presented very good results

in terms of spatial resolution, validating that this technology is useful for applications in small animal imaging using ^{125}I and also in comparison with the 2x2 flat panel array cameras. This is probably due to the continuous positioning.

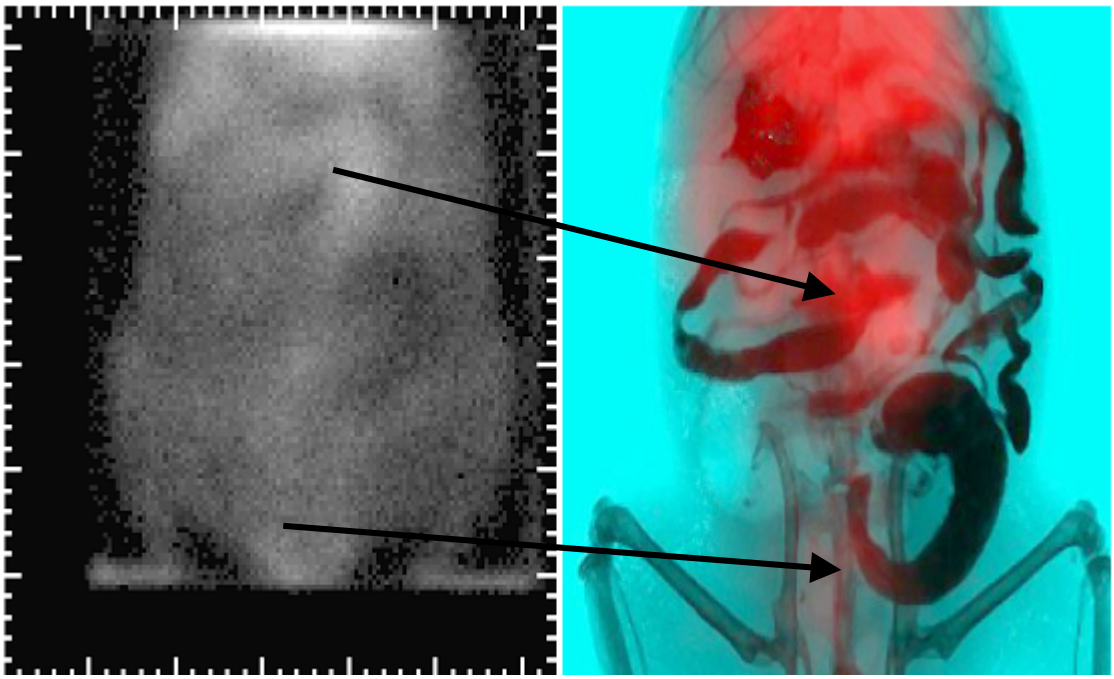

Figure 37R. Gamma-ray image with the NaI(Tl) integral assembly detector and dual modality image of the 30 μCi mouse 2 h after the injection. The upper arrow indicates the bowel inflammation tract, and the lower arrow indicates the zone of the bladder. (Be/Cu high efficiency collimator).

Conclusions

The aim of present thesis is an experimentation of new technologies and methodologies for single photon (SPE) imaging in Nuclear Medicine In particular in the field of breast cancer diagnosis, the job was finalized to the realization of a Gamma Camera with high spatial resolution and large FOV, within Integrated Mammographic Imaging project. In fact, the realized gamma camera prototype with high spatial resolution may be considered the more advanced detector in term of technology and high performances, available at the moment in Europe. Moreover, even if dedicated to the breast cancer diagnosis, the camera represents a technological reference for future planning of gamma camera dedicated to the scintigraphic diagnosis also for other organs, like prostate or thyroid, based on modular detector.

The high values of energy resolution (15 % in active zone and 20% in dead zone @140 keV without LUT procedure) and intrinsic spatial resolution, 1 mm FWHM, respect to 3,7 mm in Anger Camera, have allowed to improve SNR value, in the breast cancer diagnosis, until to a maximum of 80% and the visualization of lesions less than 8 mm diameter, where the traditional measurement with Anger Camera failed. In Table 1C the SNR values obtained in clinical trial are shown, in function of lesion diameter, for Anger Camera and high resolution prototype.

Table 1C
SNR results

Lesion (mm)	**SNR Anger Camera**	**SNR High spat.resol. Camera**
0.5< Ø <0.8	Non visible	7 ± 1
0.8< Ø <1.5	6 ± 1	22 ± 4
Ø > 1.5	8 ± 1	36 ± 6

In order to improve the contrast of scintimammography images in collaboration with the University of Ferrara a method of multivariate analysis (MIA) algorithm was implemented. The analysis of multivariate image allows to differentiate in the images the contribute due to the Compton scattering

The results show the real possibility to reduce the scintimammographic data in images defined principal component where the Compton radiation and the region involved in the tumoral lesion are considered like separate images. This separation allows to improve the image quality, in terms of contrast, especially in the zones with high scattering contribution coming from the chest. Moreover the algorithm allows to

visualize, according to an opportune energy windowing, morphologic detail of breast (nipple, lactiferous ducts) with uptake typically smaller respect to the tumoral lesions.

Like highlighted in the beginning of this paragraph, the aim of present thesis is the experimentation of new technologies and methodologies for SPE imaging. In the last 10 years the researchers effort to realize more specific radiotracers, respect to MIBI, has been particularly consisting even if clinical experimentations are not begun still. On the contrary the new technologies about the realization of new gamma detector utilized in this thesis can give a relevant contribute in a pre-clinical stage of experimentation on small animals. About this, in collaboration with the University and Jefferson Laboratory of Virginia (USA), a new very high resolution prototype of gamma cameras was developed and tested, that represents the future in the development of Gamma Camera. The detector is based on a particular optical coupling between a planar scintillation crystal, 1.5 mm NaI(Tl) thickness, and a last generation position sensitive photomultiplier, H8500 Hamamatsu Flat Panel, in order to remove the optical window of scintillator.

This detector, taking advantage by the continuous planar crystal response, allows to recover detection efficiency until 40% respect to a crystal array, that it is penalized by the dead zones between single pixel. Because of the low efficiency @ 140 keV, only 25% due to low scintillator thickness, the detector was involved in an *in vivo* experiment of small animal imaging where the radiotracer was ^{125}I (27 keV). The results were particularly impressive, especially in terms of anatomical details visibility and high spatial resolution, also after 2 hours by radiotracer administration and for low activity (30 μCi) mouse. Consequently overcoming the technological difficulties about this particular crystal-PSPMT assembling, the use of new prototypes of position sensitive photomultiplier with a greater number of anodes (256) could represent the new frontier about development of Gamma Camera with highest spatial resolution

Bibliography

Introduction

1. Bonadonna G, Hortobagy GN, Gianni A.M.: Textbook of breast cancer. A Clinical Guide to Therapy. Martin Dunitz, London 1997
2. Bonadonna G, Robustelli della Cuna G: Medicina Oncologica. Masson 1994 V edizione
3. Buscombe JR, Cwikla JB, Thakrar DS et al. Uptake of Tc-99m MIBI related to tumor size and type. Anticancer Research 1997, 17: 1693-1694
4. Chiu ML, Kronange JF, Piwnika-Worms D: Effect of mitochondrial and plasma membrane potentials on accumulation of hexakis (2methoxy-isobutil isonitrile) technetium in cultured mouse fibroblasts. J.Nucl Med 1990. 31: 1646-1653
5. Crane PD, Onthank DC, Bourque Cret al. Autoadiography and radioscintigraphy of technetium-99m-sestamibi in c-neu transgenic mice. J.Nucl.Med. 1995, 36: 1862-1868
6. Delmon-Moingeon LI, Piwnica-Worms D, Van Ven Abbeele AD et al: Uptake of the cation hexakis (2methoxy-isobutil isonitrile)-technetium-99m by human carcinoma cell lines in vitro. Cancer Res. 1990, 50: 2148-2202
7. Diggles L, Mena I, Khalkhali I. et al. Technical aspects of prone dependent-breast scintimammography. J.Nucl.Med Technol. 1994, 22: 165-170
8. Dupont W, Page DL. Risk factors for breast cancer in women with proliferative breast disease. N.Engl.J.Med 1985, 312: 146-151
9. Elmore JG, Barton MB, Moceri VM, Polk S, Arena PJ, Fletcher SW: Ten-year risk of false positive screening mammograms and clinical breast examinations. N Engl J Med 1998 Apr 16;338(16):1089-96
10. Fraser Symmans W, Weg N, Gross J et al. A prospective comparison of stereotaxic fine-needle aspiration versus stereotaxic core needle biopsy for the diagnosis of mammographic abnormalities. Cancer 1999,85: 1119-1132
11. Gopal B. Saha: Fundamentals of Nuclear Pharmacy III edition Springer-Verlag, New York 1992
12. Khalkhali I, Mena I, Jouanne I et al: Prone scintimammography in patients with suspicion of carcinoma of the breast. J.Am.Coll.Surg. 1994, 178: 491-497

13. Kopans DB The positive predictive value of mammography. AJR 1992: 158: 521-526
14. Meyer JE, Eberlin TJ, Stomper PC, Sonnenfeld MR: Biopsy of occult breast lesions. Analysis of 1261 abnormalities. JAMA 1990: 263: 2341-2343
15. Muller ST, Guth-Tougelids B, Creutzig GH: Imaging of malignant tumors with Tc-99m MIBI SPECT: Eur.J.Nucl.Med. 1987, 28: 562
16. Omar WS, Eissa S, Moustafa H et al: Role of Thallium-201 Chloride and Tc-99m Metoxy-Isobutyl-Isonitrile (sestaMIBI) in Evaluation of Breast Masses: Correlation with the Immunoistochemical Characteristic Prameters (Ki-67, PCNA, Bcl-2 and Angiogenesis)in Malignant Lesions. Anticancer Research 1997, 17: 1639-1644
17. Piwnica-Worms D, Chiu ML, Budding M et al: Functional imaging of multidrug-resistant P-glycoprotein with an organotechnetium complex. Cancer Res. 1993, 53:977-984
18. R P Highnam et al., "Estimation of compressed breast thickness during mammography", The British Journal of Radiology, 71 (1998), 646-653
19. Scopinaro F, Schillaci O, Scarpini M et al. Technetium-99m Sestamibi: an indicator of breast cancer invasiveness: Eur.J.Nucl.Med 1994, 21: 984-987
20. Shtern F., "Digital Mammography and Related Techniques: A perspective From the National Cancer Institute", Radiology, 183, pp-629, 1992.
21. Sickles EA: Mammographic features of 300 consecutive nonpalpable breast cancers. AJR 1986: 146: 661-663
22. Taillefer R. The role of 99mTc-Sestamibi and other conventional radiotracers in breast cancer diagnosis. Seminars in Nucl.Med 1999,1: 16-40
23. Veronesi U, Banfi A, Salvatori B et al: Breast conservation is the treatment of choice in small breast cancer: long-term results of a randomized trial. Eur. J. Cancer 1990,26:668-670
24. Waxman AD, Ramanna L, Memsic LD et al: Thallium scintigraphy in the evaluation of mass abnomalities of the breast. J. Nucl.Med 1993, 34: 18-23
25. Wingo PA, Tong T, Golden S: Cancer statistics. 1995 CA Cancer J.Clin 1995, 45: 8-30
26. Stefanin A. et al., An example of technological transfer:The IMI project, Nucl.Instr.and Meth 2004; A 518:512-516

1. “Performance Measurement of Scintillation Cameras”. Standard Publication No. NUI, Washington DC: National Electrical Manufacturers Association, 2001.
2. Anger HO. Sensitivity, resolution and linearity of the scintillation camera. IEEE Transaction on Nuclear Science 1966; 13: 380-392
3. Blasse G. Luminescence and scintillation mechanism in inorganic scintillators. Heavy scintillators, proceedings of the Crystal 2000 Workshop Chamonis, Sept 1992
4. G. F. Knoll, “Radiation Detection and Measurements”, John Wiley & Sons, New York, 2000.
5. Hal O. Anger, “Scintillation Camera”, The Review of Scientific Instruments, volume29, Number1, January 1958
6. Hendee W. R. & Ritenour R., “Medical Imaging Physics”, St. Louis, MO: Mosby Year Book, 1992, 781 pp.
7. Henkin R.E. et al. (eds.), “Nuclear Medicine”, Mosby, St. Louis, 1996.
8. J.A.Sorenson and M.E.Phelps “Physics in Nuclear Medicine” Grune & Stratton 1985
9. Moses W., “Overview of Nuclear Medical Imaging Instrumentation and Techniques“, AIP Conference Proceedings, Vol. 450(1), pp. 477-488, 1998.
10. Moses W., “Scintillator Requirements for Medical Imaging”, Proceedings of The International Conference on Inorganic Scintillators and Their Applications: SCINT99 (Edited by V. Mikhailin), Moscow, Russia, pp. 11-21, 1999.
11. Phelps M. E. et al., “Physics in Nuclear Medicine”, Grune & Stratton, New York, 1980.
12. Rogers J.G. et al., “Design of an Efficient Position Sensitive Gamma Ray Detector for Nuclear Medicine”, Phys. Med. Biol., 31:1061-1090, 1986.
13. Sandler M. P., Coleman R. E., Wackers F. J. T. et al., “Diagnostic Nuclear Medicine”, Baltimore, MD: Williams & Wilkins, 1996, 1549 pp.
14. Speller S. e Royle G., “Current status and requirements for position-sensitive detectors in medicine” Nucl. Instr. And Meth. in Phys. Res. A 477 (2002) 469-474.
15. Barone LM, Blazek K, Bollini D, Del Guerra A, de Notaristefani F, De Vincentis G, Di Domenico G, Galli M, Maly P, Pani R, Pellegrini R, Pergola A, Piffanelli A, Scopinaro F, Soluri A, Vittori F. Toward a nuclear medicine with sub-millimeter

spatial resolution. Nuclear Instuments and methods in Physics Research 1995; A 360: 302-306

16. Blazek K, de Notaristefani F, De Vincentis G, Malatesta T, Pani R, Pellegrini R, Soluri A, Scopinaro F. The effect of radiation transport on spatial resolution. Eur.J.Nucl.Med, 1993; 20 (10): 854 abstr
17. de Notaristefani F, Pani R, Barone LM, Blazek K, Bollini D, Del Guerra A, De Vincentis G, Di Domenico G, Galli M, Giganti M, Malatesta T, Maly P, Pellegrini R, Pergola A, Piffanelli A, Scopinaro F, Soluri A, Vittori F, Zavattini G. Light yield and response function of YAP:Ce multicrystal detector. International Conference on Inorganic Scintillators and Applications, Delft, The Netherlands, 1995: Scint 95 Proceedings
18. de Notaristefani F, Pani R, Scopinaro F, Blazek K, Pellegrini R, Maly P, Soluri A, Pergola A, Barone L, De Vincentis G. Malatesta T, Vittori F. YAP camera: a small field gamma camera with submillimiter spatial resolution. Eur.J.Nucl.Med, 1995; 22 (8): 337 .
19. de Notaristefani F., Pani R, Scopinaro F,.Barone LM, Blazek K, De Vincentis G, Malatesta T, Maly P, Pellegrini R, Pergola A, Soluri A, Vittori F. First results from YAP:Ce gamma camera for small animal studies. Nuclear Science Symposium and Medical Imaging Conference, San Francisco, 1995 Conference record.
20. G.De Vincentis et al., "99mTcMIBI Scintimammography with a High Resolution Single Tube Gamma Camera: Preliminary Study", Anticancer Research 17:1627-1630(1997)
21. Leo W.R., "Techniques for Nuclear Physics Experiments", Springer Verlag, 1986/2000.
22. Pani R, de Notaristefani F, Barone LM, Blazek K, Del Guerra A, De Vincentis G, Di Domenico G, Malatesta T, Maly P, Pellegrini R, Pergola A, Soluri A, Vittori F, Zavattini G, Scopinaro F. Performance studies of YAP:Ce crystal pillars for imaging applications in nuclear medicine, Nuclear Science Symposium and Medical Imaging Conference, San Francisco, 1995 Conference record.
23. Pani R, de Notaristefani F, Blazek K, Maly P, Pellegrini R, Pergola A, Soluri A, Scopinaro F. Multy-crystal Yap:Ce detector system for position sensitive measurements. Nucl.Instr.and Meth 1994; A 348:551-558
24. Pani R, De Vincentis G, Scopinaro F, Pellegrini R, Soluri A,.Weinberg IN, Pergola A, Scafè R, Trotta G. Dedicated gamma camera for Single Photon Emission

Mammography (SPEM). IEEE Transaction on Nuclear Science 1998, 45 (6): 3127-3133,

25. Pani R, Pellegrini R, Scopinaro F, Soluri A, De Vincentis G, Pergola A., Corona A., Filippi S., Ballesio PL, Grammatico A. Scintillating array gamma camera for clinical use. Nucl.Instr. & Meth. A 1997, 392: 295-298
26. Pani R, Pellegrini R, Soluri A, Safè R, De Vincentis G, Cinti MN, Indovina L, Trotta G, Lanconelli N, Bollini D. Detector module of a single photon compact ring tomograph for high resolution breast imaging Proceedings of WC 2000-Mondial Medical Physics World Congress, 2000
27. Pani R, Pergola A, Pellegrini R, Soluri A, De Vincentis G, Filippi S, Di Domenico G, Del Guerra A, Scopinaro F. New generation position sensitive PMT for nuclear medicine imaging Nucl.Instr. & Meth. A 1997, 392: 319-323
28. Pani R, Scopinaro F, Depaola G, Pellegrini R, Soluri A. Very high resolution gamma camera based on position sensitive photomultiplier tube. Physica Medica 1993; IX (2-3): 233-236
29. Pani R., Scafè R. et al., "Scintillation Arrays Characterization for Photon Emission Imaging", Nucl. Inst. Meth. in Phys., Sez. A, 477(1-3): 72-77, 2003.
30. Pellegrini R, Pani R, Scopinaro F, A.Soluri, Pergola A, De Vincentis G, Ierardi M, Weinberg IN. Single photon emission mammography (SPEM) with high resolution, single tube gamma camera. Radionuclides for mammary gland current status and future aspects Mediterra publishers, Athens, 1997: 149-154
31. Royle NE, Royle GJ, Pani R, Speller R: Design of high resolution collimators for small gamma cameras. Nuclear Science Symposium and Medical Imaging Conference, San Francisco,1995 Conference record.
32. Scopinaro F, De Vincentis G, Pani R, Pellegrini R, Banci M, Soluri A, Massa R, Bruno I, de Notaristefani F, Centi Colella A. YAP camera: perspectives in radiopharmacological research. Eur.J.Nucl.Med, 1995; 22 (8): 599
33. Scopinaro F, Pani R, De Vincentis G, Soluri A, Pellegrini R, Porfiri LM. High resolution scintimammography improves the accuracy of 99mTc sestamibi scintimammography: use of a new dedicated gamma camera Eur. J. Nucl. Med., 1999 26: 1279-1288
34. Weinberg IN, Pani R, Pellegrini R, Scopinaro F, De Vincentis G, Pergola A, Soluri A.. Small lesion visualization in scintimammography. IEEE Transactions on Nuclear Science, Vol 44 No 3, June 1997 1398-1402

35. C. Bonifazzi, A. Tartari, M. N. Cinti, L. Nanetti, R. Pellegrini, and R. Pani., Description of the response in scintillation crystal arrays: analytical vs. statistical approaches , Nuclear Instruments and Methods in Physics Research B, 213C, 231-235, (2004)
36. P. Geladi and H. Grahn, Multivariate Image Analysis, Wiley, N.Y., (1996).
37. C. Bonifazzi, A. Tartari et al. Multivariate image analysis of ECoSP Compton spectra, Nucl. Instr. Meth. B, 213, 712-716 (2004).
38. J. Huang et al., Multi-way methods in image analysis: relationship and application, Chem. Intel. Lab. System, ; 66, 141-158, (2003).

Experimental Equipment

1. Hamamatsu, Technical Sheet R8520-00C12 PSPMT, Japan, 2002
2. Stefanin A. et al., An example of technological transfer:The IMI project, Nucl.Instr.and Meth 2004; A 518:512-516
3. Pani R. et al., The ‘‘IMI’’ project: an advanced gamma camera for scintimammography, Nucl.Instr.and Meth 2004; A 518:380-381
4. Relazione finale del progetto Imaging Mammografico Integrato, Linea 4: Scintimammografia, Responsabile Scientifico Prof. A. Stefanini, 2004.
5. Hamamatsu, Technical Sheet R8500 Flat Panel PSPMT, Japan, 2004
6. Rutherford Appleton Laboratories Microelectronics Group, HX2/RAL/SS Technical Data Sheet
7. National AT-MIO/A1 E Series User Manual, 1996